

Topology optimization for surface flows

Yongbo Deng^{1*}, Weihong Zhang^{2†}, Jihong Zhu²,
Junqiang Bai³, Zhenyu Liu⁴, Jan G. Korvink^{5‡}

1 State Key Laboratory of Applied Optics,
Changchun Institute of Optics, Fine Mechanics and Physics,
Chinese Academy of Sciences, 130033 Changchun, China;

2 State IJR Center of Aerospace Design and Additive Manufacturing,
Northwestern Polytechnical University, 710072 Xi'an, China;

3 Institute of Intelligence Material and Structure,
Unmanned System Research Institute,
Northwestern Polytechnical University, 710072 Xi'an, China;

4 Changchun Institute of Optics, Fine Mechanics and Physics,
Chinese Academy of Sciences, 130033 Changchun, China;

5 Institute of Microstructure Technology (IMT),
Karlsruhe Institute of Technology (KIT),
Hermann-von-Helmholtzplatz 1,
76344 Eggenstein-Leopoldshafen, Germany.

July 7, 2022

Abstract

This paper presents a topology optimization approach for surface flows, which can represent the viscous and incompressible fluidic motions at the solid/liquid and liquid/vapor interfaces. The fluidic motions on such material interfaces can be described by the surface Navier-Stokes equations defined on 2-manifolds or two-dimensional manifolds, where the elementary tangential calculus is implemented in terms of exterior differential operators expressed in a Cartesian system. Based on the topology optimization model for fluidic flows with porous medium filling the design domain, an artificial Darcy friction is added to the area force term of the surface Navier-Stokes equations and the physical area forces are penalized to eliminate their existence in the fluidic regions and to avoid the invalidity of the porous medium model. Topology optimization for steady and unsteady surface flows can be implemented by iteratively evolving the impermeability of the porous medium on the 2-manifolds, where the impermeability is interpolated by the material density derived from a design variable. The related partial differential equations are solved by using the surface finite element method. Numerical examples have been provided to demonstrate this topology optimization approach for surface flows, including the boundary velocity driven flows, area force driven flows and convection-diffusion flows.

Keywords: Topology optimization; Surface flow; Material distribution method; Porous medium model.

1 Introduction

The viscous dissipation of an object moving in a fluid is mainly caused by the slip boundary condition at the solid/fluid interface corresponding to the surface of the object. The slip boundary condition can be categorized into no slip, partial slip and complete slip types as demonstrated in Fig. 1. The solid/fluid interface is essentially slippery. Increasing the slip length can effectively reduce the shear stress led by the velocity gradient at the solid/fluid interface and thereby decrease the viscous dissipation. Usually, the slip length at the solid/fluid interface is small enough with an ignorable value, and such solid/fluid interface can be regarded as no-slip boundary. When the slip length is prone to infinity, it can be approximated as a complete-slip

*yongbo_deng@hotmail.com (Y. Deng)

†zhangwh@nwpu.edu.cn (W. Zhang)

‡jan.korvink@kit.edu (J.G. Korvink)

boundary. Several approaches have been developed to approximate the complete-slip boundary condition, including chemically coating or physically structuring the solid/liquid interfaces to derive extreme hydrophobicity [1], using the optimal control method to manipulate the boundary velocity of flows [2] and producing a vapor layer between the solid and liquid phases based on the Leidenfrost phenomenon [3]. The fluidic velocity is tangential to the complete-slip boundary, and it has zero gradient in the normal direction of the object surface. The complete-slip boundary is a streamsurface of the bulk flow around the object. The fluidic flow at the complete-slip boundary can thus be separated as a surface flow demonstrated in Fig. 2(a).

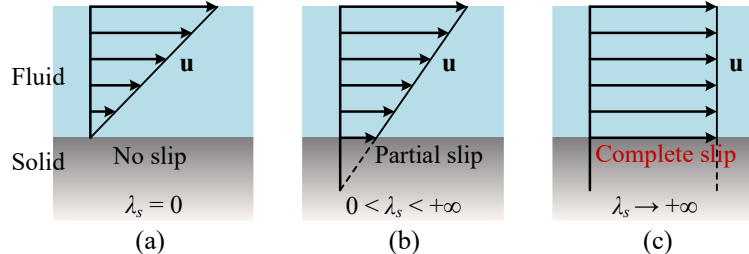


Figure 1: Sketch for the no slip, partial slip and complete slip boundary conditions at the solid/fluid interfaces, where \mathbf{u} is the fluidic velocity and λ_s is the slip length.

Moreover, several interfacial phenomena, including mass transfer on biological membranes, open flows and sealed flows of flexible microfluidics, can also be described as surface flows. On a biological membrane, the mass transfer process can be investigated as the dynamics of a corresponding surface flow of a liquid at the mid-surface of the membrane [4], where the membrane is fixed on the skeletons composed of materials in the solid phase and sandwiched by the liquid/vapor interfaces. In flexible microfluidics [5], a surface flow plays the key roles on the functional performance of a deformed, bent and stretched device, which can overcome the drawbacks, including relatively expensive processing, brittle and not self-sealing, associated with the usually used materials of silicon and glass. For an open flow of flexible microfluidics, a surface flow corresponds to the mass transfer process at the free liquid/vapor interface of the flow in a unsealed groove-shaped channel [6]. For a flexible microfluidic flow sealed by the walls with complete slip property, a surface flow can be used to describe the mass transfer process in the mid-surface of the sealed flow.

The above introduced flows can be described as surface flows on curved surfaces, which can be represented by 2-manifolds (Fig. 2(b)). Surface flows can extend the design space of fluidic structures onto material interfaces including solid/liquid and liquid/vapor interfaces. **Because reasonable surface patterns can effectively reduce the viscous dissipation of flows and the drag forces of objects, this paper presents a topology optimization approach for surface flows, to implement the robust and efficient inverse design of structures on the extended design space.**

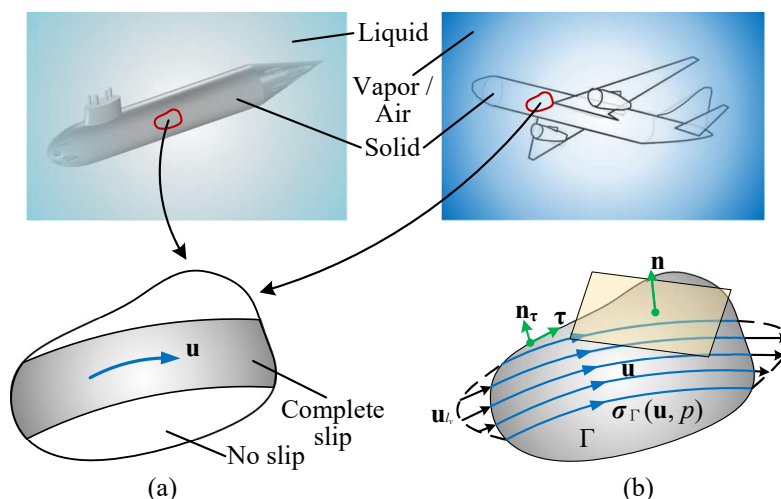


Figure 2: (a) Sketch for the flows corresponding to objects moving in fluids with complete-slip boundaries. (b) Sketch for the surface flow on a 2-manifold. In the sketches, Γ is the 2-manifold, σ_Γ is the Boussinesq-Scriven surface stress tensor, \mathbf{u} is the fluidic velocity, p is the fluid pressure, \mathbf{u}_{l_v} is the known fluidic velocity at the boundary of Γ , \mathbf{n} is the unitary normal vector of Γ , $\boldsymbol{\tau}$ is the unitary tangential vector at $\partial\Gamma$ and $\mathbf{n}_\tau = \mathbf{n} \times \boldsymbol{\tau}$ is the outward unitary normal at $\partial\Gamma$.

This topology optimization approach is implemented by using the material distribution method, which was pioneered by Bendsøe and Kikuchi for elasticity [7] and has been extended to several other scientific fields [8]. Surface flows are important aspects of fluid mechanics. With regard to fluid mechanics, topology optimization has been implemented for Stokes flows [9], steady Navier-Stokes flows [10], creeping fluid flows [11], unsteady Navier-Stokes flows [12, 13], flows with body forces [14, 15], turbulent flows [16, 17], two-phase flows of immiscible fluids [18], electroosmotic flows [19, 20] and flows of non-Newtonian fluids [21, 22], etc.; and topology optimization for fluidic flows have been reviewed in [23]. With regard to material interfaces, researches have been implemented for stiffness and multi-material structures [24–30], layouts of shell structures [31–36], electrode patterns of electroosmosis [20], fluid-structure and fluid-particle interaction [37–39], energy absorption [40], cohesion [41], actuation [42] and wettability control [43–45], etc.; a topology optimization approach implemented on 2-manifolds has also been generally developed with applications in the fields of wettability control, heat transfer and electromagnetics [46].

Surface flows can be described by the surface Navier-Stokes equations defined on 2-manifolds representing the material interfaces [47–52]. This can be dated back to Scriven who was interested in the interface rheology on a foam [47]. In topology optimization for flows problems, a porous medium model was developed for Stokes flows [9]. This model was then extended to implement topology optimization for steady Navier-Stokes flows [10] and unsteady Navier-Stokes flows [12, 13]. In this model, the porous medium was filled in the two-/three-dimensional design domains; correspondingly, an artificial Darcy friction was introduced into the force terms of the Stokes equations and Navier-Stokes equations. The impermeability of the porous medium was evolved in the topology optimization procedure to derive the geometrical configurations of the fluidic structures. Inspired by the porous medium model developed in [9], this paper implements topology optimization for surface flows by filling a porous medium onto the 2-manifolds. Correspondingly, an artificial Darcy friction is added to the area force term of the surface Navier-Stokes equations.

To solve the surface flow problems on the 2-manifolds filled with the surface porous medium, surface finite element methods can be used to discretize the surface Navier-Stokes equations, where a Lagrange multiplier method and a penalty technique have been developed to enforce the tangentiality constraints of the flow fields [53, 54]. Because the Lagrange multiplier method can ensure more accurate enforcement of the tangentiality constraints, it is chosen to solve the surface Navier-Stokes equations. Based on the porous medium model and the surface finite element method, the topology optimization approach is formulated for the unsteady surface flows. This approach can be reduced into the forms for the steady surface flows by setting the flow fields to be independent of time.

The remained sections of the paper are organized as follows. In Section 2, a monolithic description of the topology optimization problem for the surface flows is presented. In Section 3, numerical implementation for the iterative solution of the topology optimization problem is introduced. In Section 4, numerical examples are provided to demonstrate the developed topology optimization approach for the surface flows. In Section 5 and 6, the conclusion and acknowledgment of this paper are provided. In Section 7, details are provided for the surface finite element discretization of the related partial differential equations (PDEs). All the mathematical descriptions are implemented in a Cartesian system.

2 Methodology

In this section, a topology optimization problem for the incompressible surface flows is described by using the material distribution method.

2.1 Surface Navier-Stokes equations

The equations of the motion of a Newtonian surface fluid can be formulated intrinsically on a 2-manifold of codimension one in an Euclidian space sketched in Fig. 2(b). In the incompressible cases, the constitutive law of the Newtonian surface fluid is

$$\boldsymbol{\sigma}_\Gamma = -p\mathbf{P} + \mu(\nabla_\Gamma\mathbf{u} + \nabla_\Gamma\mathbf{u}^T) \text{ at } \forall \mathbf{x} \in \Gamma, \quad (1)$$

where Γ is the 2-manifold loaded with fluid flows; ∇_Γ is the tangential gradient operator on Γ ; $\boldsymbol{\sigma}_\Gamma$ is the Boussinesq-Scriven surface stress tensor [55, 56]; \mathbf{u} is the fluidic velocity; p is the fluidic pressure; μ is the shear viscosity of the fluid on Γ ; the superscript T represents the operator for the transposition of a tensor; $\mathbf{P} = \mathbf{I} - \mathbf{nn}^T$ is the normal projector on the tangential space at $\mathbf{x} \in \Gamma$, with \mathbf{x} denoting a node on Γ ; \mathbf{I} is the three-dimensional unitary tensor; \mathbf{n} is unitary normal vector of Γ . Based on the conservation laws of momentum and mass, the surface Navier-

Stokes equations can be derived to describe the incompressible surface flows:

$$\rho \left[\frac{\partial \mathbf{u}}{\partial t} + (\mathbf{u} \cdot \nabla_{\Gamma}) \mathbf{u} \right] = -\nabla_{\Gamma} p + \operatorname{div}_{\Gamma} [\mu (\nabla_{\Gamma} \mathbf{u} + \nabla_{\Gamma} \mathbf{u}^T)] + \mathbf{b}_{\Gamma} \left. \vphantom{\rho} \right\} \text{ at } \forall (t, \mathbf{x}) \in (0, T) \times \Gamma, \quad (2)$$

$$-\operatorname{div}_{\Gamma} \mathbf{u} = 0$$

where ρ is the fluid density; \mathbf{b}_{Γ} is the area forces in the tangential spaces of Γ ; $\operatorname{div}_{\Gamma}$ is the tangential divergence operator; T is the terminal time. The evolution of time t from 0 to T together with the 2-manifold Γ defines a 3-manifold (three-dimensional manifold) $S := (0, T) \times \Gamma$ sketched in Fig. 3. Because the fluid spatially flows on the 2-manifold Γ , the fluidic velocity is a vector in the tangential space of Γ , and it satisfies a tangential constraint:

$$\mathbf{u} \cdot \mathbf{n} = 0 \text{ at } \forall (t, \mathbf{x}) \in (0, T) \times \Gamma. \quad (3)$$

To solve the surface Navier-Stokes equations for the unsteady incompressible surface flows, an initial condition with a specified spatial distribution of the fluidic velocity is required, and it is expressed as

$$\mathbf{u}|_{t=0} = \mathbf{u}_0 \text{ at } \forall \mathbf{x} \in \Gamma, \quad (4)$$

where \mathbf{u}_0 is a specified distribution of the fluidic velocity on Γ .

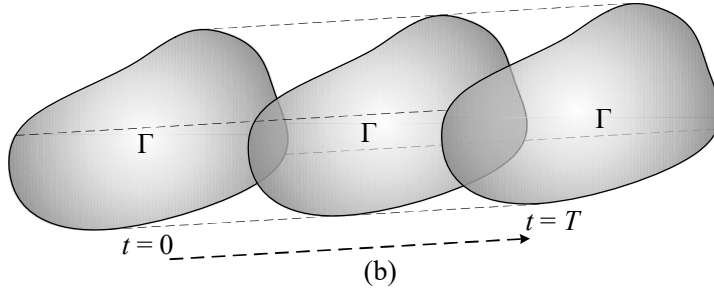


Figure 3: Sketch for the 3-manifold $S := (0, T) \times \Gamma$ defined by the time interval $(0, T)$ and the 2-manifold Γ , with T representing the terminal time.

To solve the surface Navier-Stokes equations, the fluidic velocity and pressure are also required to be specified at some boundaries, interfaces or points of a 2-manifold. The following boundary, interface or point conditions are considered in this paper. The inlet or interfacial boundary condition with known fluidic velocity is expressed as

$$\mathbf{u} \cdot \mathbf{n}_{\tau} = \mathbf{u}_{l_v} \cdot \mathbf{n}_{\tau} \left. \vphantom{\mathbf{u}} \right\} \text{ at } \forall (t, \mathbf{x}) \in (0, T) \times l_v, \quad (5)$$

$$\mathbf{u} - (\mathbf{u} \cdot \mathbf{n}_{\tau}) \mathbf{n}_{\tau} = \mathbf{u}_{l_v} - (\mathbf{u}_{l_v} \cdot \mathbf{n}_{\tau}) \mathbf{n}_{\tau}$$

where \mathbf{u}_{l_v} is a known distribution of the fluidic velocity; l_v satisfies $l_v \subset \partial\Gamma$ when l_v is a boundary curve of Γ , and it satisfies $l_v \subset \Gamma$ when l_v is an interface curve of Γ ; $\mathbf{n}_{\tau} = \mathbf{n} \times \boldsymbol{\tau}$ is the outward unitary normal at $\partial\Gamma$, with $\boldsymbol{\tau}$ representing the unitary tangential vector at $\partial\Gamma$. To ensure the compatibility between Eqs. 3 and 5, the known fluidic velocity \mathbf{u}_{l_v} should be a distribution satisfying $\mathbf{u}_{l_v} \cdot \mathbf{n} = 0$. When the known fluidic velocity is $\mathbf{0}$, Eq. 5 degenerates into the no-slip boundary condition:

$$\mathbf{u} \cdot \mathbf{n}_{\tau} = 0 \left. \vphantom{\mathbf{u}} \right\} \text{ at } \forall (t, \mathbf{x}) \in (0, T) \times l_{v0}, \quad (6)$$

$$\mathbf{u} - (\mathbf{u} \cdot \mathbf{n}_{\tau}) \mathbf{n}_{\tau} = \mathbf{0}$$

where \mathbf{u}_{l_v} is equal to $\mathbf{0}$ on $l_{v0} \subset l_v$, and l_{v0} is the no-slip part of the boundary curve. The open boundary condition with zero tangential stress is expressed as

$$\boldsymbol{\sigma}_{\Gamma} \cdot \mathbf{n}_{\tau} = \mathbf{0} \text{ at } \forall (t, \mathbf{x}) \in (0, T) \times l_s, \quad (7)$$

where l_s is the boundary satisfying $l_s \subset \partial\Gamma$. The point condition with known fluid pressure is expressed as

$$p = p_0 \text{ at } \forall (t, \mathbf{x}) \in (0, T) \times \mathcal{P}, \quad (8)$$

where p_0 is a known fluid pressure; $\mathcal{P} \subset \Gamma$ is a finite point set.

The variational formulation of the surface Navier-Stokes equations is considered in the functional spaces without containing the tangential constraint of the fluidic velocity. The tangential constraint of the fluidic velocity is imposed by a Lagrangian multiplier. Based on the Galerkin

method, the variational formulation of the surface Navier-Stokes equations can be derived in the form of the following initial value problem:

$$\begin{aligned}
& \text{find } \begin{cases} \mathbf{u} \in (\mathcal{V}(S))^3 \text{ with } \begin{cases} \mathbf{u} - (\mathbf{u} \cdot \mathbf{n}_\tau) \mathbf{n}_\tau = \mathbf{u}_{l_v} - (\mathbf{u}_{l_v} \cdot \mathbf{n}_\tau) \mathbf{n}_\tau \text{ at } \forall (t, \mathbf{x}) \in (0, T) \times l_v, \\ \mathbf{u}|_{t=0} = \mathbf{u}_0 \text{ at } \forall \mathbf{x} \in \Gamma, \end{cases} \\ p \in \mathcal{V}(S) \text{ with } p = p_0 \text{ at } \forall (t, \mathbf{x}) \in (0, T) \times \mathcal{P}, \\ \lambda \in \mathcal{W}(S) \text{ with } \lambda = 0 \text{ at } \forall (t, \mathbf{x}) \in (0, T) \times l_v, \end{cases} \\
& \text{such that } \int_0^T \int_\Gamma \rho \left[\frac{\partial \mathbf{u}}{\partial t} + (\mathbf{u} \cdot \nabla_\Gamma) \mathbf{u} \right] \cdot \tilde{\mathbf{u}} + \frac{\mu}{2} (\nabla_\Gamma \mathbf{u} + \nabla_\Gamma \mathbf{u}^T) : (\nabla_\Gamma \tilde{\mathbf{u}} + \nabla_\Gamma \tilde{\mathbf{u}}^T) \\
& - p \operatorname{div}_\Gamma \tilde{\mathbf{u}} + \mathbf{u} \cdot \nabla_\Gamma \tilde{p} - \mathbf{b}_\Gamma \cdot \tilde{\mathbf{u}} + \lambda (\tilde{\mathbf{u}} \cdot \mathbf{n}) + \tilde{\lambda} (\mathbf{u} \cdot \mathbf{n}) \, d\Gamma dt - \int_0^T \int_{l_v} \mathbf{u}_{l_v} \cdot \mathbf{n}_\tau \tilde{p} \, dl dt \\
& - \int_0^T \int_{\partial\Gamma \setminus l_v} \mathbf{u} \cdot \mathbf{n}_\tau \tilde{p} \, dl dt = 0, \text{ for } \forall \tilde{\mathbf{u}} \in (\mathcal{V}(S))^3, \forall \tilde{p} \in \mathcal{V}(S) \text{ and } \forall \tilde{\lambda} \in \mathcal{W}(S),
\end{aligned} \tag{9}$$

where λ is the Lagrange multiplier used to impose the tangential constraint of the fluidic velocity; $\tilde{\mathbf{u}}$, \tilde{p} and $\tilde{\lambda}$ are the test functions of \mathbf{u} , p and λ , respectively; $d\Gamma$ and dl are the differential of the 2-manifold and its boundary curves, respectively; $\mathcal{V}(S)$ represents the Hilbert space defined as $\mathcal{H}((0, T); \mathcal{H}(\Gamma)) = \{u(t, \mathbf{x}) : u(t, \mathbf{x})|_{\mathbf{x}=\mathbf{x}_0} \in \mathcal{H}((0, T)), u(t, \mathbf{x})|_{t=t_0} \in \mathcal{H}(\Gamma), \partial u/\partial t \in \mathcal{L}^2((0, T); \mathcal{H}(\Gamma)), \text{ for } \forall t_0 \in (0, T), \forall \mathbf{x}_0 \in \Gamma\}$, with $\mathcal{L}^2((0, T); \mathcal{H}(\Gamma)) := \{u(t, \mathbf{x}) : u(t, \mathbf{x})|_{\mathbf{x}=\mathbf{x}_0} \in \mathcal{L}^2((0, T)), u(t, \mathbf{x})|_{t=t_0} \in \mathcal{H}(\Gamma), \text{ for } \forall t_0 \in (0, T), \forall \mathbf{x}_0 \in \Gamma\}$; $\mathcal{W}(S)$ represents the Hilbert space defined as $\mathcal{L}^2((0, T); \mathcal{L}^2(\Gamma)) := \{u(t, \mathbf{x}) : u(t, \mathbf{x})|_{\mathbf{x}=\mathbf{x}_0} \in \mathcal{L}^2((0, T)), u(t, \mathbf{x})|_{t=t_0} \in \mathcal{L}^2(\Gamma), \text{ for } \forall t_0 \in (0, T), \forall \mathbf{x}_0 \in \Gamma\}$; $\mathcal{H}((0, T))$ and $\mathcal{H}(\Gamma)$ represent the first order Sobolev spaces defined on $(0, T)$ and Γ , respectively; $\mathcal{L}^2((0, T))$ and $\mathcal{L}^2(\Gamma)$ represent the second order Lebesgue spaces defined on $(0, T)$ and Γ , respectively.

On the Lagrangian multiplier in Eq. 9, it is used to impose the tangential constraint of the fluidic velocity and acts as a distributed force in the normal direction of the 2-manifold. When the fluidic particles cooperatively move on the 2-manifold, the centrifugal, Coriolis and Euler forces are induced by the non-zero distribution of the curvature of the 2-manifold. Those forces have the components in the normal direction of the 2-manifold, i.e., the normal components of the centrifugal, Coriolis and Euler forces. The normal components of the forces are cancelled out by the distributed force corresponding to the Lagrangian multiplier. The tangential constraint of the fluidic velocity is thus satisfied.

The above surface Navier-Stokes equations and the corresponding variational formulation are introduced for unsteady surface flows. For the steady surface flows, the time dependence is casted off by removing the local-derivative term $\partial \mathbf{u}/\partial t$ from Eq. 2. Sequentially, the time-space 3-manifold S degenerates into the spacial 2-manifold Γ ; the initial condition in Eq. 4 is unnecessary; all the time dependence is removed from the tangential constraint in Eqs. 3 and the boundary, interface and point conditions in Eqs. 5, 7 and 8; the time integration of the variational formulation in Eq. 9 is removed; and the related functions are located in the first order Sobolev space $\mathcal{H}(\Gamma)$ and Lebesgue space $\mathcal{L}^2(\Gamma)$ instead of $\mathcal{V}(S)$ and $\mathcal{W}(S)$.

2.2 Porous medium model

In this topology optimization for surface flows, a porous medium model is utilized heuristically [9]. In this model, a porous medium is filled onto the 2-manifold. Correspondingly, an artificial Darcy friction is added into the area force term of the surface Navier-Stokes equations in Eq. 2. The artificial Darcy friction is derived based on the constitutive law of the porous medium. It is assumed to be proportional to the fluidic velocity [9, 10], i.e.,

$$\mathbf{b}_a = -\alpha \mathbf{u} \text{ at } \forall \mathbf{x} \in \Gamma, \tag{10}$$

where α is the impermeability. When the porosity of the filled medium is zero, it corresponds to a solid material with infinite impermeability and zero fluidic velocity caused by the infinite friction force. When the porosity is infinite, it corresponds to the structural void for the transport of the fluid with zero impermeability. Therefore, the impermeability can be described as

$$\alpha = \begin{cases} +\infty & \text{for } \gamma_p = 0, \\ 0 & \text{for } \gamma_p = 1, \end{cases} \tag{11}$$

where $\gamma_p \in \{0, 1\}$ is a binary distribution defined on Γ , with 0 and 1 representing the solid and fluid phases, respectively. To avoid the difficulty on solving a binary optimization problem, the binary variable γ_p is relaxed to vary continuously in $[0, 1]$. The relaxed binary variable is referred to as the material density of the impermeability.

Fluidic structures are invariable for the flow problems, although the fluidic velocity and pressure can vary along with time in the unsteady flows. The material density of the impermeability is independent of time. The material density is obtained by sequentially implementing the surface-PDE filter and the threshold projection on a time-independent design variable valued continuously in $[0, 1]$, in order to remove the gray regions and control the minimum length scale in a derived fluidic structure. Inspired by the PDE filter developed in [57], the surface-PDE filter for the design variable is implemented by solving the following surface PDE [46]:

$$\begin{cases} -\operatorname{div}_\Gamma (r_f^2 \nabla_\Gamma \gamma_f) + \gamma_f = \gamma \text{ at } \forall \mathbf{x} \in \Gamma, \\ \mathbf{n}_\tau \cdot \nabla_\Gamma \gamma_f = 0 \text{ at } \forall \mathbf{x} \in \partial\Gamma, \end{cases} \quad (12)$$

where γ is the design variable; γ_f is the filtered design variable. The variational formulation of the surface-PDE filter is considered in the first order Sobolev space defined on Γ . It can be derived based on the Galerkin method:

$$\begin{aligned} &\text{find } \gamma_f \in \mathcal{H}(\Gamma) \text{ for } \gamma \in \mathcal{L}^2(\Gamma), \text{ such that} \\ &\int_\Gamma r_f^2 \nabla_\Gamma \gamma_f \cdot \nabla_\Gamma \tilde{\gamma}_f + \gamma_f \tilde{\gamma}_f - \gamma \tilde{\gamma}_f \, d\Gamma = 0 \text{ for } \forall \tilde{\gamma}_f \in \mathcal{H}(\Gamma), \end{aligned} \quad (13)$$

where $\tilde{\gamma}_f$ is the test function of γ_f . The threshold projection of the filtered design variable is [58, 59]

$$\gamma_p = \frac{\tanh(\beta\xi) + \tanh(\beta(\gamma_f - \xi))}{\tanh(\beta\xi) + \tanh(\beta(1 - \xi))}, \quad (14)$$

where r_f is the filter radius and it is constant; β and ξ are the parameters for the threshold projection, with values chosen based on numerical experiments [59].

Based on the description of the impermeability in Eq. 11 and the derivation of the material density in Eqs. 12 and 14, the material interpolation of the impermeability can be implemented as [9]

$$\alpha(\gamma_p) = \alpha_f + (\alpha_s - \alpha_f) q \frac{1 - \gamma_p}{q + \gamma_p}, \quad (15)$$

where α_s and α_f are the impermeability of the solid and fluid phases, respectively; q is the parameter used to tune the convexity of this interpolation. For the fluid phase, the impermeability is zero, i.e., $\alpha_f = 0$. For the solid phase, α_s should be infinite theoretically; numerically, a finite value much larger than the fluid density ρ is chosen for α_s , to ensure the stability of the numerical implementation and approximate the solid phase with enough accuracy. Based on numerical tests, q is valued as 10^{-1} , and α_s is chosen as $10^4 \rho$ to satisfy $\alpha_s \gg \rho$.

For the porous medium model, the area force term in the surface Navier-Stokes equations includes the artificial Darcy friction and physical area force:

$$\mathbf{b}_\Gamma = -\alpha \mathbf{u} + \chi \mathbf{b}_p, \quad (16)$$

where \mathbf{b}_p is the physical area force, and it can be the gravity, centrifugal force along with Coriolis and Euler forces in a rotating frame, etc.; χ is a penalizing factor imposed on \mathbf{b}_p . It has been specified that the physical forces can drive the fluid flow in the approximated solid phase with high impermeability [15]. This can result in the invalidity of the porous medium model. To solve this problem, a penalization is implemented by multiplying the physical force \mathbf{b}_p with the penalizing factor expressed as

$$\chi(\gamma_p) = \chi_{\max} + (\chi_{\min} - \chi_{\max}) q \frac{1 - \gamma_p}{q + \gamma_p}, \quad (17)$$

where $\chi_{\min} = 0$ and $\chi_{\max} = 1$ are the minimal and maximal values of χ , respectively. The effect of the penalization is to achieve the physical retrieval by gradually removing the physical force from solid phase and keeping its existence in the liquid phase. Then, the problem on the invalidity of the porous medium model can be avoided, when a physical force exists.

2.3 Topology optimization problem

Based on the introduction of the surface Navier-Stokes equations and the porous medium model, the topology optimization problem of surface flows can be constructed in the following general

form:

find $\gamma : \Gamma \mapsto [0, 1]$ to minimize or maximize $\frac{J}{J_0}$ with

$$J = \int_0^T \int_{\Gamma} A(\mathbf{u}, \nabla_{\Gamma} \mathbf{u}, p; \gamma_p) d\Gamma dt + \int_0^T \int_{\partial\Gamma} B(\mathbf{u}, p) dl dt + \int_{\Gamma} C(\mathbf{u}; \gamma_p) \Big|_{t=T} d\Gamma,$$

constrained by

$$\left\{ \begin{array}{l} \left\{ \begin{array}{l} \rho \left[\frac{\partial \mathbf{u}}{\partial t} + (\mathbf{u} \cdot \nabla_{\Gamma}) \mathbf{u} \right] = -\nabla_{\Gamma} p + \operatorname{div}_{\Gamma} [\mu (\nabla_{\Gamma} \mathbf{u} + \nabla_{\Gamma} \mathbf{u}^T)] - \alpha \mathbf{u} + \chi \mathbf{b}_p \\ -\operatorname{div}_{\Gamma} \mathbf{u} = 0 \\ \mathbf{u} \cdot \mathbf{n} = 0 \end{array} \right\} \text{ at } \forall (t, \mathbf{x}) \in S \\ \alpha(\gamma_p) = \alpha_f + (\alpha_s - \alpha_f) q \frac{1 - \gamma_p}{q + \gamma_p} \\ \chi(\gamma_p) = \chi_{\max} + (\chi_{\min} - \chi_{\max}) q \frac{1 - \gamma_p}{q + \gamma_p} \\ \left\{ \begin{array}{l} -\operatorname{div}_{\Gamma} (r_f^2 \nabla_{\Gamma} \gamma_f) + \gamma_f = \gamma, \text{ at } \forall \mathbf{x} \in \Gamma \\ \mathbf{n}_{\tau} \cdot \nabla_{\Gamma} \gamma_f = 0, \text{ at } \forall \mathbf{x} \in \partial\Gamma \end{array} \right. \\ \gamma_p = \frac{\tanh(\beta\xi) + \tanh(\beta(\gamma_f - \xi))}{\tanh(\beta\xi) + \tanh(\beta(1 - \xi))} \\ |v - v_0| \leq 10^{-3} \text{ with } v = \frac{1}{|\Gamma|} \int_{\Gamma} \gamma_p d\Gamma \quad (\text{Area constraint}) \end{array} \right. , \quad (18)$$

where J is the design objective in a general form; A , B and C are the integrands of J ; J_0 is the value of J corresponding to the initial distribution of the design variable; to regularize this optimization problem, an area constraint with a permitted tolerance of 10^{-3} chosen to be much less than 1 is imposed on the fluidic structure; v is the area fraction of the fluidic structure; $v_0 \in (0, 1)$ is the specified area fraction; $|\Gamma| = \int_{\Gamma} 1 d\Gamma$ is the area of Γ .

The topology optimization problem in Eq. 18 is formulated for the unsteady surface flows. For the steady surface flows, reduction can be implemented by setting the related variables to be independent of time. The time integration in the design objective J is casted off, and the surface integration term about C defined at the terminal time $t = T$ is removed; the surface Navier-Stokes equations in the constraints are degenerated into the stationary ones.

2.4 Adjoint analysis

The topology optimization problem in Eq. 18 can be solved by using a gradient information-based iterative procedure, where the adjoint sensitivities are used to determine the relevant gradient information. The adjoint analysis is implemented for the design objective and the area constraint to derive the adjoint sensitivities.

Based on the adjoint analysis method [60], the adjoint sensitivity of the design objective J can be derived as

$$\delta J = -T \int_{\Gamma} \gamma_{fa} \delta \gamma d\Gamma, \quad (19)$$

where δ is the operator for the first order variational of a variable; $\delta \gamma \in \mathcal{L}^2(\Gamma)$ is first order variational of γ ; γ_{fa} is the adjoint variable of the filtered design variable γ_f . The adjoint variable γ_{fa} can be derived from the adjoint equations in the variational formulations. The variational formulation for the adjoint equations of the surface Navier-Stokes equations is derived in the form of a terminal value problem described as

$$\begin{aligned}
& \text{find } \begin{cases} \mathbf{u}_a \in (\mathcal{V}(S))^3 \text{ with } \begin{cases} \mathbf{u}_a - (\mathbf{u}_a \cdot \mathbf{n}_\tau) \mathbf{n}_\tau = \mathbf{0} \text{ at } \forall (t, \mathbf{x}) \in (0, T) \times l_v, \\ \mathbf{u}_a|_{t=T} = -\frac{1}{\rho} \frac{\partial C}{\partial \mathbf{u}} \text{ at } \forall \mathbf{x} \in \Gamma, \end{cases} \\ p_a \in \mathcal{V}(S) \text{ with } p_a = 0 \text{ at } \forall (t, \mathbf{x}) \in (0, T) \times \mathcal{P}, \\ \lambda_a \in \mathcal{W}(S) \text{ with } \lambda_a = 0 \text{ at } \forall (t, \mathbf{x}) \in (0, T) \times l_v, \end{cases} \\
& \text{such that } \int_0^T \int_\Gamma \frac{\partial A}{\partial \mathbf{u}} \cdot \tilde{\mathbf{u}}_a + \frac{\partial A}{\partial \nabla_\Gamma \mathbf{u}} : \nabla_\Gamma \tilde{\mathbf{u}}_a + \frac{\partial A}{\partial p} \tilde{p}_a - \rho \frac{\partial \mathbf{u}_a}{\partial t} \cdot \tilde{\mathbf{u}}_a \\
& + \rho [(\tilde{\mathbf{u}}_a \cdot \nabla_\Gamma) \mathbf{u} + (\mathbf{u} \cdot \nabla_\Gamma) \tilde{\mathbf{u}}_a] \cdot \mathbf{u}_a + \frac{\mu}{2} (\nabla_\Gamma \mathbf{u}_a + \nabla_\Gamma \mathbf{u}_a^T) : (\nabla_\Gamma \tilde{\mathbf{u}}_a + \nabla_\Gamma \tilde{\mathbf{u}}_a^T) \\
& + \left(\alpha \mathbf{I} - \chi \frac{\partial \mathbf{b}_p}{\partial \mathbf{u}} \right) \mathbf{u}_a \cdot \tilde{\mathbf{u}}_a + \mathbf{u}_a \cdot \nabla_\Gamma \tilde{p}_a - p_a \operatorname{div}_\Gamma \tilde{\mathbf{u}}_a + (\tilde{\lambda}_a \mathbf{u}_a + \lambda_a \tilde{\mathbf{u}}_a) \cdot \mathbf{n} \, d\Gamma \, dt \\
& - \int_0^T \int_{\partial \Gamma} \left(\mathbf{u}_a \cdot \mathbf{n}_\tau - \frac{\partial B}{\partial p} \right) \tilde{p}_a \, dl \, dt + \int_0^T \int_{\partial \Gamma \setminus l_v} \frac{\partial B}{\partial \mathbf{u}} \cdot \tilde{\mathbf{u}}_a \, dl \, dt = 0, \\
& \text{for } \forall \tilde{\mathbf{u}}_a \in (\mathcal{V}(S))^3, \forall \tilde{p}_a \in \mathcal{V}(S) \text{ and } \forall \tilde{\lambda}_a \in \mathcal{W}(S),
\end{aligned} \tag{20}$$

where \mathbf{u}_a , p_a and λ_a are the adjoint variables of \mathbf{u} , p and λ , respectively; $\tilde{\mathbf{u}}_a$, \tilde{p}_a and $\tilde{\lambda}_a$ are the test functions of \mathbf{u}_a , p_a and λ_a , respectively. The adjoint equation of the surface-PDE filter is derived in the variational formulation as

$$\begin{aligned}
& \text{find } \gamma_{fa} \in \mathcal{H}(\Gamma), \text{ such that} \\
& \frac{1}{T} \int_0^T \int_\Gamma \left(\frac{\partial A}{\partial \gamma_p} + \frac{\partial \alpha}{\partial \gamma_p} \mathbf{u} \cdot \mathbf{u}_a - \frac{\partial \chi}{\partial \gamma_p} \mathbf{b}_p \cdot \mathbf{u}_a \right) \frac{\partial \gamma_p}{\partial \gamma_f} \tilde{\gamma}_{fa} \, d\Gamma \, dt + \frac{1}{T} \int_\Gamma \frac{\partial C}{\partial \gamma_p} \Big|_{t=T} \frac{\partial \gamma_p}{\partial \gamma_f} \tilde{\gamma}_{fa} \, d\Gamma \\
& + \int_\Gamma r_f^2 \nabla_\Gamma \gamma_{fa} \cdot \nabla_\Gamma \tilde{\gamma}_{fa} + \gamma_{fa} \tilde{\gamma}_{fa} \, d\Gamma = 0, \text{ for } \forall \tilde{\gamma}_{fa} \in \mathcal{H}(\Gamma),
\end{aligned} \tag{21}$$

where $\tilde{\gamma}_{fa}$ is the test function of γ_{fa} .

The adjoint sensitivity of the area fraction v can be derived as

$$\delta v = -\frac{1}{|\Gamma|} \int_\Gamma \gamma_{fa} \delta \gamma \, d\Gamma, \tag{22}$$

where γ_{fa} can be derived from the following variational formulation for the adjoint equation of the surface-PDE filter:

$$\begin{aligned}
& \text{find } \gamma_{fa} \in \mathcal{H}(\Gamma), \text{ such that} \\
& \int_\Gamma \frac{\partial \gamma_p}{\partial \gamma_f} \tilde{\gamma}_{fa} + r_f^2 \nabla_\Gamma \gamma_{fa} \cdot \nabla_\Gamma \tilde{\gamma}_{fa} + \gamma_{fa} \tilde{\gamma}_{fa} \, d\Gamma = 0, \text{ for } \forall \tilde{\gamma}_{fa} \in \mathcal{H}(\Gamma).
\end{aligned} \tag{23}$$

After the derivation of the adjoint sensitivities in Eqs. 19 and 23, the design variable γ can be evolved iteratively to inversely design a fluidic structure on a 2-manifold.

The adjoint analysis is implemented on the topology optimization problem for the unsteady surface flows. It can be changed into the form for the steady surface flows by implementing reductions. For the steady surface flows, reductions can be implemented directly based on the time-independence of the fluidic velocity and pressure, with casting off the surface integration term about C defined at the terminal time $t = T$ and degenerating the functional spaces into the ones defined on Γ instead of S .

3 Numerical implementation

The topology optimization problem in Eq. 18 is solved by using an iterative procedure described as the pseudocode in Table 1, where a loop is included for the iterative solution of the topology optimization problem in Eq. 18. The surface finite element method is utilized to solve the variational formulations of the relevant PDEs and adjoint equations [61]. The 2-step backward differentiation formula (BDF) is utilized to discretize the time derivative terms of the variational formulations [62]. The details for the surface finite element solution have been provided in Appendix 7. To ensure the well-posedness of the variational formulations of the surface Navier-Stokes equations and their adjoint equations (Eqs. 9 and 20), Taylor-Hood elements are used to satisfy the inf-sup condition [63]. To ensure the efficiency and positivity of the design variable, linear elements are used to interpolate and solve the variational formulations of the surface-PDE filter and its adjoint equation (Eqs. 13, 21 and 23). The finite element nodes of the Taylor-Hood and linear elements of the quadrangular-element based discretization of a 2-manifold have been sketched in Fig. 4.

In the iterative procedure, the radius of the surface-PDE filter is set as $\pi/30$; the projection parameter β with the initial value of 1 is doubled after every 30 iterations; the loop is stopped

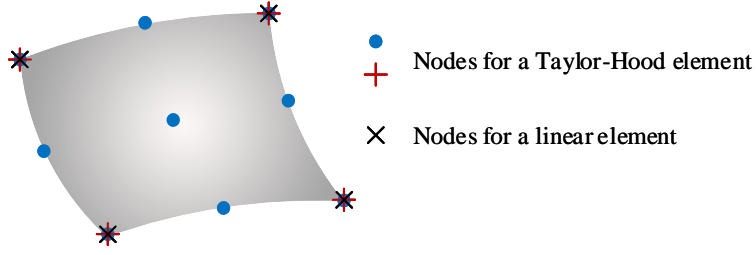


Figure 4: Sketch for the finite element nodes of the Taylor-Hood and linear elements of the quadrangular-element based discretization of the 2-manifold Γ .

Algorithm 1: iterative solution of Eq. 18

Set $\mathbf{u}_0, \mathbf{u}_{l_v}, p_0, \rho, \mu$ and v_0 ;

$$\text{Set } \begin{cases} \gamma \leftarrow v_0 \\ n_{\max} \leftarrow 315 \\ n_i \leftarrow 1 \\ \xi \leftarrow 0.5 \\ \beta \leftarrow 1 \end{cases} \quad \text{and} \quad \begin{cases} \alpha_{\min} \leftarrow 0 \\ \alpha_{\max} \leftarrow 10^4 \rho \\ \chi_{\min} \leftarrow 0 \\ \chi_{\max} \leftarrow 1 \\ q \leftarrow 10^{-1} \end{cases};$$

loop

Solve Eq. 13 to derive γ_f by filtering γ ;
 Project γ_f to derive γ_p and compute v ;
 Solve \mathbf{u}, p and λ from Eq. 9, and evaluate J/J_0 ;
 Solve $\mathbf{u}_a, p_a, \lambda_a$ and γ_{fa} from Eqs. 20 and 21;
 Evaluate δJ from Eq. 19;
 Solve γ_{fa} from Eq. 23;
 Evaluate δv from Eq. 22;
 Update γ based on δJ and δv ;

if $\text{mod}(n_i, 30) == 0$

$\beta \leftarrow 2\beta$;

end if

$$\text{if } (n_i == n_{\max}) \text{ or } \begin{cases} \beta == 2^{10} \\ \frac{1}{5} \sum_{m=0}^4 |J_{n_i} - J_{n_i-m}| / J_0 \leq 10^{-3} \\ |v - v_0| \leq 10^{-3} \end{cases}$$

break;

end if

$n_i \leftarrow n_i + 1$

end loop

Table 1: Pseudocode used to solve the topology optimization problem of surface flows. In the iterative solution loop, n_i is the loop-index, n_{\max} is the maximal value of n_i , J_{n_i} is the value of J in the n_i -th iteration, and mod is the operator used to take the remainder.

when the maximal iteration number is reached, or if the averaged variation of the design objective in continuous 5 iterations and the residual of the area constraint are simultaneously less than the specified tolerance 10^{-3} chosen to be much less than 1. The design variable is updated by using the method of moving asymptotes [64].

4 Results and discussion

In this section, topology optimization for surface flows is implemented on the 2-manifolds with and without boundary. For the 2-manifolds without boundary, the orientable 2-manifolds are chosen as the sphere and torus and the non-orientable 2-manifold is chosen as the Möbius strip. The density and dynamic viscosity of the fluid are assigned to be unitary.

4.1 Steady surface flows driven by boundary velocity

In this section, topology optimization is implemented for the steady surface flows driven by boundary velocity. The 2-manifolds corresponding to continuously deforming quadrangular planes into the shapes of a sphere, a torus and a Möbius strip are considered (Fig. 5). In the sketched continuously deforming process, the 2-manifolds with boundaries are evolved into the ones without boundary and the areas of the 2-manifolds are kept to be constant. In Fig. 5, the inlet boundaries with known velocity distributions, the no-slip boundaries and the open boundaries have been marked in different colors. The known velocity distributions are the parabolic functions of the arc-length coordinate of the inlet boundaries. The known velocity \mathbf{u}_{l_v} in Eq. 5 satisfies $\sup_{\mathbf{x} \in l_v} |\mathbf{u}_{l_v}| = 1$ and the tangential constraint in Eq. 3. By setting the design objective as the power of the viscous dissipation described as

$$J = \int_{\Gamma} \frac{\mu}{2} (\nabla_{\Gamma} \mathbf{u} + \nabla_{\Gamma} \mathbf{u}^T) : (\nabla_{\Gamma} \mathbf{u} + \nabla_{\Gamma} \mathbf{u}^T) + \alpha \mathbf{u}^2 d\Gamma, \quad (24)$$

the optimized structure of the surface flows on the 2-manifolds in Fig. 5 are derived as shown in Figs. 6, 7 and 8, where the area fraction of the area constraint is specified as $v_0 = 0.4$.

The derived surface structures on the quadrangular planes shown in Figs. 6(a), 7(a) and 8(a) are consistent with the previously reported diffuser-shaped channels derived by using the topology optimization approach for 2D fluidic flows [9, 10]. When the square plane deforms as demonstrated in Figs. 5(a1-a5), the diffuser-shaped channel in Fig. 6(a) is split into two branches as shown in Figs. 6(b-e). When the rectangular plane deforms as demonstrated in Figs. 5(b1-b5), the diffuser-shaped channel in Fig. 7(a) is firstly rolled and then bent as shown in Figs. 7(b-e). When the rectangular plane deforms into a Möbius strip as demonstrated in Figs. 5(c1-c3), the derived surface channel in Fig. 8(a) is winded into a twisted channel and a Möbius strip as shown in Figs. 8(b) and 8(c). The inherent mechanism for the evolution of the optimized surface structures is that the fluid is prone to moving in the short path between the inlet and outlet to minimize the viscous dissipation.

Topology optimization for the steady surface flows has been further implemented to maximize the projected velocity distribution perpendicular or parallel to a specified distribution of the unitary directional vectors. For the 2-manifolds sketched in Figs. 5(b3-b5), the specified unitary directional vectors are the ones tangential to the axial curves of the cylinder, semi-torus and torus. The design objective is set to maximize

$$J = \int_{\Gamma} [\mathbf{u} - (\mathbf{u} \cdot \mathbf{d}) \mathbf{d}]^2 d\Gamma, \quad (25)$$

where \mathbf{d} is the specified unitary directional vectors tangential to the axial curves of the cylinder and semi-torus. For the 2-manifolds sketched in Figs. 5(c1-c3), topology optimization is implemented to maximize the projected velocity distribution parallel to the directional vector \mathbf{k} shown in Fig. 5. The design objective is set to maximize

$$J = \int_{\Gamma} (\mathbf{u} \cdot \mathbf{k})^2 d\Gamma. \quad (26)$$

The results are then derived as shown in Figs. 9, where helical-/zigzag-shaped surface structures are obtained on the cylinder, semi-torus, torus, rectangular strip, twisted strip and Möbius strip, respectively. The derived helical/zigzag structures can preserve the mass and momentum conservation of the surface flows and maximize the projected velocity component, simultaneously. Those structures have chirality and lose the geometrical symmetry of the 2-manifolds to avoid the elimination of the velocity component in the direction of the specified directional vectors. This ensures the transporting continuity of the surface flows on the 2-manifolds.

To confirm the optimized performance of the structures derived for the steady surface flows, the results in Figs. 7(c-e), 8(a-c) and 9(a-f) are cross compared as listed in Table 2. From

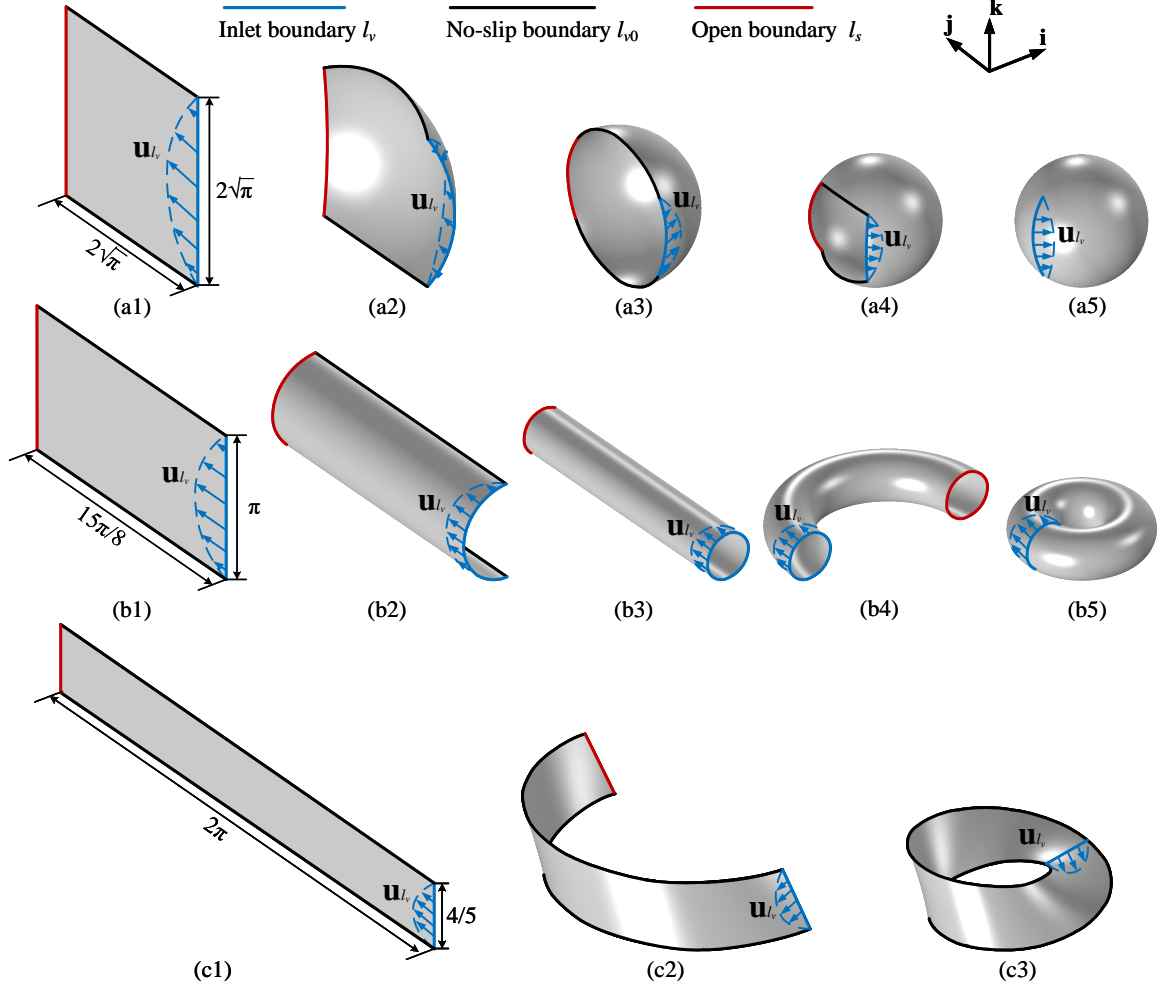


Figure 5: (a1-a5) 2-manifolds corresponding to continuously deforming a square plane into the shape of a sphere, discretized by 60×60 quadrangular elements. (b1-b5) 2-manifolds corresponding to continuously deforming a rectangular plane into the shape of a torus, discretized by 60×112 quadrangular elements. (c1-c3) 2-manifolds corresponding to deforming a rectangular strip into the shape of a Möbius strip, discretized by 30×240 quadrangular elements. During the deformation process, the areas of the 2-manifolds are kept to be constant. The inlet boundaries with known velocity distributions, no-slip boundaries and open boundaries have been marked in blue, black and red colors, respectively. \mathbf{u}_{l_v} , satisfying the tangential constraint of the fluidic velocity in Eq. 3, is a known velocity distribution, which is a parabolic function of the arc-length coordinate at an inlet boundary. \mathbf{i} , \mathbf{j} and \mathbf{k} are three directional vectors perpendicular to each other.

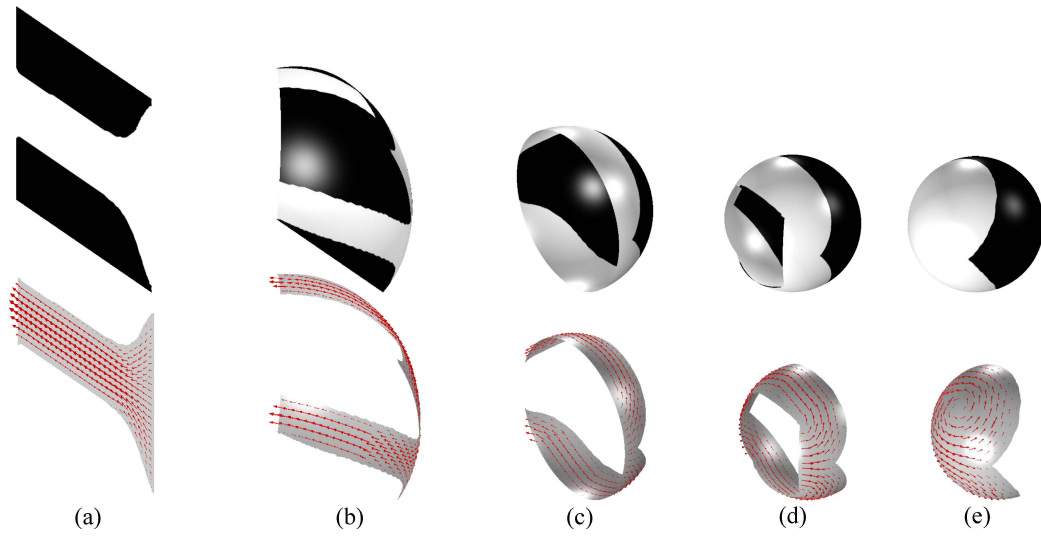


Figure 6: Topology optimization for the steady surface flows on the 2-manifolds sketched in Figs. 5(a1-a5) corresponding to continuously deforming a square plane into the shape of a sphere, where the design objective is to minimize the viscous dissipation of the surface flows driven by the inlet/interfacial velocity \mathbf{u}_{l_v} . The distributions of the material density are derived as shown in the first row. The patterns of the surface flows are derived as shown in the second row, where the distributions of the velocity vectors are presented by the arrows marked in red color.

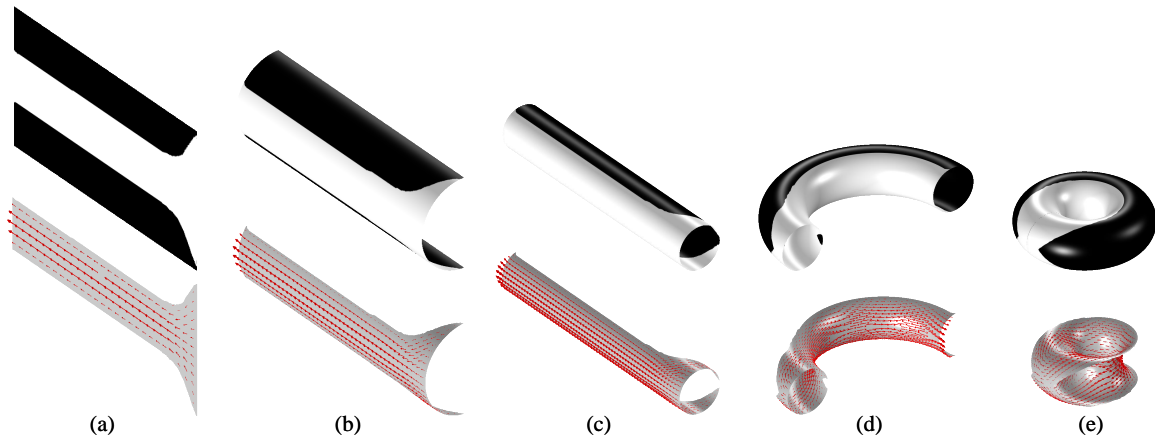


Figure 7: Topology optimization for the steady surface flows on the 2-manifolds sketched in Figs. 5(b1-b5) corresponding to continuously deforming a rectangular plane into the shape of a torus, where the design objective is to minimize the viscous dissipation of the surface flows driven by the inlet/interfacial velocity \mathbf{u}_{l_v} . The distributions of the material density are shown in the first row. The patterns of the surface flows are shown in the second row, where the distributions of the velocity vectors are presented by the arrows marked in red color.

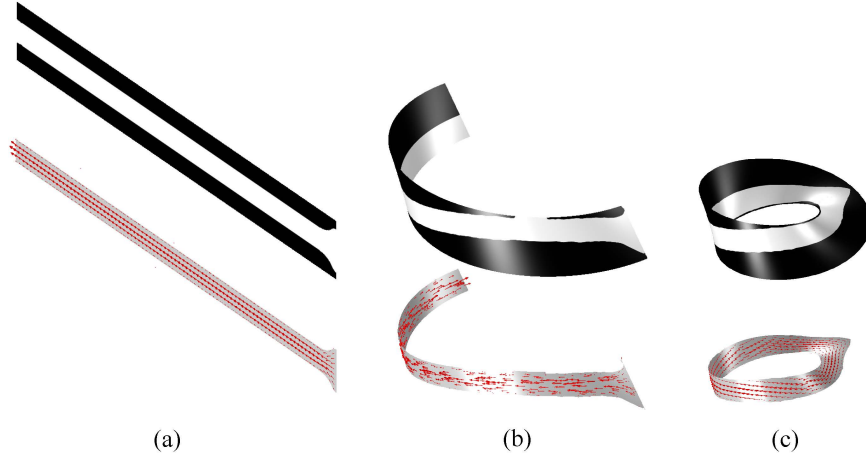


Figure 8: Topology optimization for the steady surface flows on the 2-manifolds sketched in Figs. 5(c1-c3) corresponding to deforming a rectangular strip into the shape of a Möbius strip, where the design objective is to minimize the viscous dissipation of the surface flows driven by the inlet/interfacial velocity \mathbf{u}_v . The distributions of the material density are shown in the first row. The patterns of the surface flows are shown in the second row, where the distributions of the velocity vectors are presented by the arrows marked in red color.

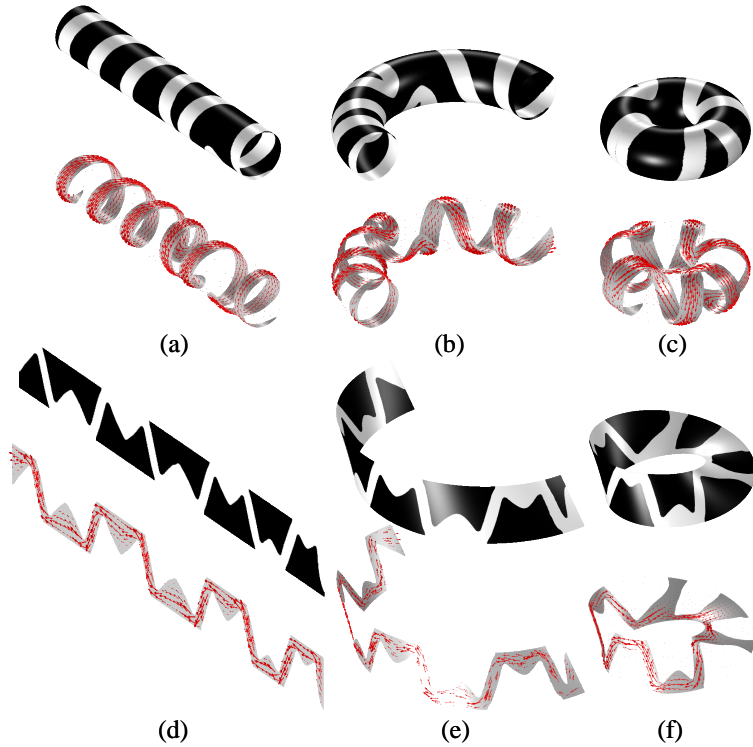


Figure 9: Topology optimization for the steady surface flows on the 2-manifolds sketched in Figs. 5(b3-b5) and 5(c1-c3), where the surface flows are driven by the inlet/interfacial velocity \mathbf{u}_v . (a-c) The design objective is to maximize the projected velocity distribution perpendicular to the directional vectors tangential to the axial curves of the cylinder, semi-torus and torus. (d-f) The design objective is to maximize the projected velocity distribution perpendicular to the directional vector \mathbf{k} shown in Fig. 5. The distributions of the material density are shown in the first row. The patterns of the surface flows are shown in the second row, where the distributions of the velocity vectors are presented by the arrows marked in red color.

Table 2, the optimized performance of the derived surface structures in Figs. 7(c-e) and 8(a-c) can be confirmed from their smaller converged values of the power of the viscous dissipation; meanwhile, the optimized performance of the derived surface structures in Figs. 9(a-f) can be confirmed from their larger converged values on the projected velocity distribution.

	Fig. 7(c)		Fig. 9(a)
Eq. 24	2.00×10^2	<	1.40×10^4
Eq. 25	4.00×10^{-1}	<	1.18×10^2
	Fig. 7(d)		Fig. 9(b)
Eq. 24	1.63×10^2	<	1.34×10^4
Eq. 25	1.12×10^0	<	1.13×10^2
	Fig. 7(e)		Fig. 9(c)
Eq. 24	2.26×10^2	<	1.19×10^4
Eq. 25	2.31×10^0	<	1.04×10^2
	Fig. 8(a)		Fig. 9(d)
Eq. 24	5.63×10^2	<	3.49×10^3
Eq. 26	1.98×10^{-2}	<	3.86×10^0
	Fig. 8(b)		Fig. 9(e)
Eq. 24	5.19×10^2	<	2.93×10^3
Eq. 26	1.11×10^{-1}	<	2.85×10^0
	Fig. 8(c)		Fig. 9(f)
Eq. 24	1.06×10^2	<	1.03×10^3
Eq. 26	3.59×10^{-2}	<	1.04×10^0

Table 2: Values of the design objectives in Eqs. 24, 25 and 26 for the surface structures in Figs. 7(c-e), 8(a-c) and 9(a-f). The optimized entries have been noted in bold.

4.2 Unsteady surface flows driven by area forces

In this section, topology optimization is implemented for the unsteady surface flows driven by area forces, which are generated by rotating the 2-manifolds around specified axes. The rotating systems have been sketched in Figs. 10(a-c). The sizes of the sphere, torus and Möbius strip are the same as that in Fig. 5. They are rotated around the axes across their centers in the direction of \mathbf{k} . In a rotating system, the area forces include the centrifugal, Coriolis and Euler forces. On a 2-manifold, the combination of the tangential components of those forces are used as the physical area force in Eq. 16 to drive the surface flows:

$$\mathbf{b}_p = (\mathbf{b}_c + \mathbf{b}_C + \mathbf{b}_E) - [(\mathbf{b}_c + \mathbf{b}_C + \mathbf{b}_E) \cdot \mathbf{n}] \mathbf{n}, \quad (27)$$

where \mathbf{b}_c , \mathbf{b}_C and \mathbf{b}_E are the centrifugal, Coriolis and Euler forces, respectively. Those forces are expressed as $\mathbf{b}_c = \rho \boldsymbol{\omega} \times \mathbf{r} \times \boldsymbol{\omega}$, $\mathbf{b}_C = \rho \mathbf{u} \times \boldsymbol{\omega}$ and $\mathbf{b}_E = \rho \mathbf{r} \times \frac{d\boldsymbol{\omega}}{dt}$, where $\boldsymbol{\omega}$ is the angular velocity; \mathbf{r} is the vector of the rotating radius; $\frac{d\boldsymbol{\omega}}{dt}$ is the angular acceleration. The time-dependent angular velocity and angular acceleration are imposed as plotted in Figs. 10(d-e).

The design destination is to optimize the actuation performance of the area forces. The design objective is thus set to maximize the work of the area forces:

$$J = \int_0^T \int_{\Gamma} \mathbf{b}_p \cdot \mathbf{u} \, d\Gamma dt. \quad (28)$$

By using the topology optimization approach introduced in Section 2, the optimized surface structures are derived as shown in Fig. 11 including the plots of the variation of the work power of the area forces along with the time evolution, where the area fraction of the area constraint is specified as $v_0 = 0.3$. The results in Fig. 11 show that the derived surface structures have the shapes of ring belts to make the combined area force exert positive work by ensuring the consistency between the directions of the combined area force and fluidic velocity. During the rotating process, the Coriolis force has zero contribution to the work of the area forces, because it is perpendicular to the local fluidic velocity; the work of the centrifugal force is much less than that of the Euler force. Therefore, the surface flows are mainly actuated by the Euler force and the graphics of the work power in Figs. 11(a3-c3) have similar shapes as that of the angular

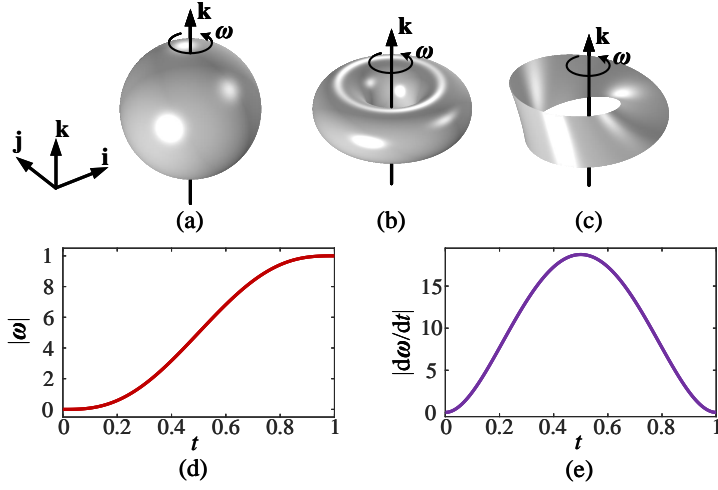


Figure 10: (a-c) 2-manifolds in the shapes of sphere, torus and Möbius strip rotating around the axes across their centers. (d-e) Time-dependent angular velocity and angular acceleration of rotated 2-manifolds. \mathbf{k} is the directional vectors of the rotating axes; $\boldsymbol{\omega}$ is the angular velocity; $d\boldsymbol{\omega}/dt$ is the angular acceleration.

acceleration plotted in Fig. 10(e). From Figs. 11(a2-c2), we can see that the directions of the combined area force and fluidic velocity on the sphere and torus are more consistent than that on the Möbius strip. The area forces have more efficient actuation performance on the sphere and torus, and the actuated surface flows have stronger convection. Therefore, the curves for the sphere and torus in Figs. 11(a3) and 11(b3) have less symmetry than that for the Möbius strip in Fig. 11(c3).

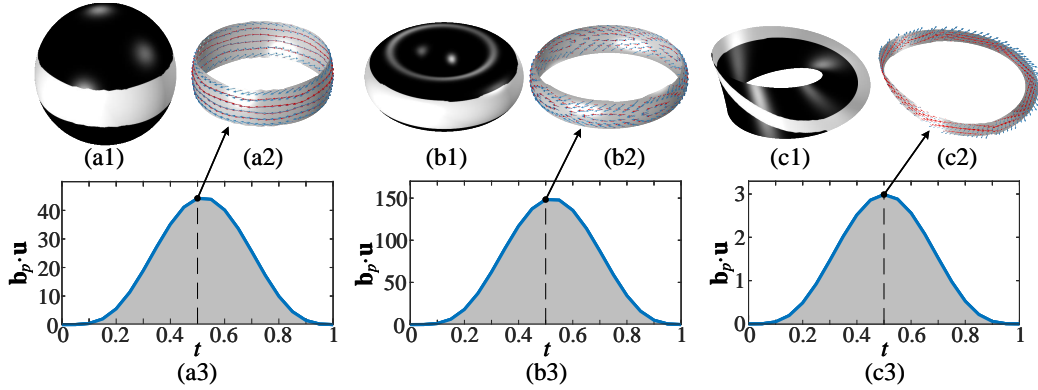


Figure 11: (a1-c1) Surface structures derived by maximizing the work of the area forces generated in the rotating systems. (a2-c2) Patterns of the surface flows, where the distributions of the velocity vectors and area forces at time $t = 0.5$ are presented by the arrows marked in red and blue colors, respectively. (a3-c3) Plots of the variation of the work power of the area forces along with the time evolution.

When the design destination is changed to maximize the projected velocity distribution in the directions of the rotating axes:

$$J = \int_0^T \int_{\Gamma} (\mathbf{u} \cdot \mathbf{k})^2 d\Gamma dt, \quad (29)$$

the optimized surface structures are derived as shown in Fig. 12, including the plots of the variation of the spatial integration of the projected velocity distribution along with the time evolution. The surface structures are derived in the shapes of the twisted rings. Those surface structures can maximize the work of the components of the area forces in the directions of the rotating axes. In Figs. 12(a3) and 12(b3), the asymmetry of the curves is also caused by the more efficient actuation performance of the area forces and stronger convection of the actuated surface flows.

To confirm the optimized performance of the structures derived for the unsteady surface flows, the results in Figs. 11 and 12 are cross compared in Table 3. From Table 3, the optimized

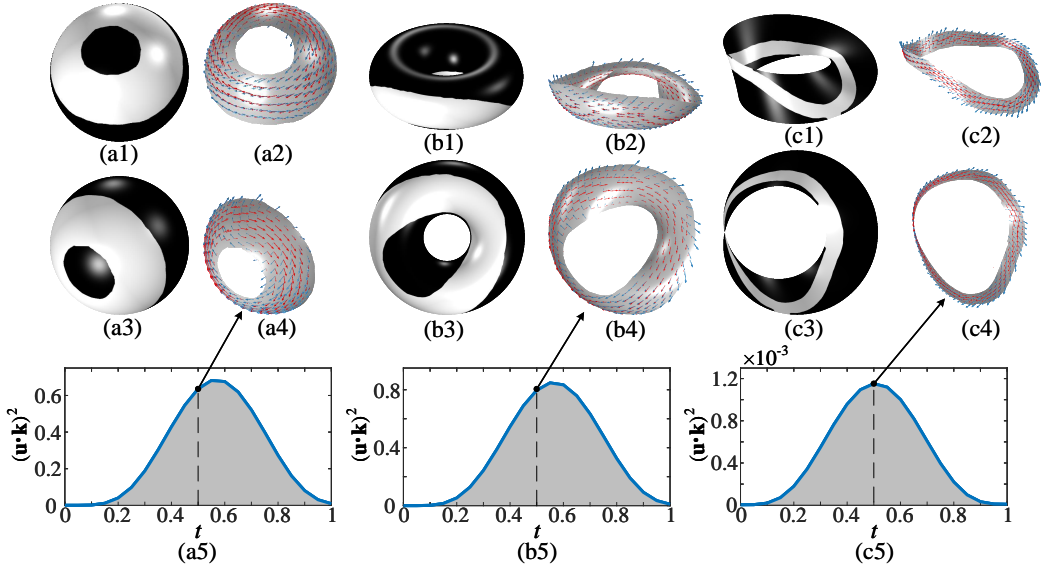


Figure 12: (a1-c1) Surface structures derived by maximizing the work of the area forces generated in the rotating systems. (a2-c2) Patterns of the surface flows, where the distributions of the velocity vectors and area forces at time $t = 0.5$ are presented by the arrows marked in red and blue colors, respectively. (a3) and (a4) are the top views of (a1) and (a2), respectively. (b3), (b4), (c3) and (c4) are the bottom views of (b1), (b2), (c1) and (c2), respectively. (a5-c5) Plots of the variation of the integration of the projected velocity distribution along with the time evolution.

performance of the derived surface structures in Fig. 11 can be confirmed from their larger converged values of the work of the area forces; meanwhile, the optimized performance of the derived surface structures in Fig. 12 can be confirmed from their larger converged values on the projected velocity distribution.

	Fig. 11(a1)	Fig. 12(a1)
Eq. 28	1.81×10^1	4.00×10^{-1}
Eq. 29	6.33×10^{-5}	2.85×10^{-1}
	Fig. 11(b1)	Fig. 12(b1)
Eq. 28	6.08×10^1	4.52×10^1
Eq. 29	1.07×10^{-3}	3.53×10^{-1}
	Fig. 11(c1)	Fig. 12(c1)
Eq. 28	1.21×10^0	1.04×10^0
Eq. 29	1.13×10^{-4}	4.67×10^{-4}

Table 3: Values of the design objectives in Eqs. 28 and 29 for the surface structures in Figs. 11 and 12. The optimized entries have been noted in bold.

4.3 Convection-diffusion problems of surface flows

Convection and diffusion are the most basic phenomena in the fluidic flows. The corresponding typical problem is the mixing of the fluid with different concentration of a solute. Topology optimization for convection-diffusion problems has been investigated in 2D plane and 3D spatial domains [67,68]. For surface flows, the convection and diffusion can be described by the surface convection-diffusion equation:

$$\text{div}_\Gamma (-D\nabla_\Gamma c) + \mathbf{u} \cdot \nabla_\Gamma c = 0 \text{ at } \forall \mathbf{x} \in \Gamma, \quad (30)$$

where c is the distribution of the concentration on the 2-manifold Γ ; D is the diffusion coefficient of the solute; the fluidic velocity \mathbf{u} is described by using the steady counterpart of the surface Navier-Stokes equations in Eq. 2, for which the known-velocity, no-slip and open boundary conditions are included. For the surface convection-diffusion equation, the distribution of the concentration is known at the boundary curve with known non-zero fluidic velocity, i.e., $c = c_0$

at $l_v \setminus l_{v0}$, where c_0 is a known distribution of the concentration; the remained part of the boundary curves is insulation boundary, i.e., $\nabla_{\Gamma} c \cdot \mathbf{n}_{\tau} = 0$ at $\partial\Gamma \setminus (l_v \setminus l_{v0})$.

The fluidic velocity \mathbf{u} in Eq. 30 can be solved from the variational formulation for the steady counterpart of the surface Navier-Stokes equations:

$$\begin{aligned} \text{find } & \begin{cases} \mathbf{u} \in (\mathcal{H}(\Gamma))^3 \text{ with } \mathbf{u} - (\mathbf{u} \cdot \mathbf{n}_{\tau}) \mathbf{n}_{\tau} = \mathbf{u}_{l_v} - (\mathbf{u}_{l_v} \cdot \mathbf{n}_{\tau}) \mathbf{n}_{\tau} \text{ at } \forall \mathbf{x} \in l_v \\ p \in \mathcal{H}(\Gamma) \\ \lambda \in \mathcal{L}^2(\Gamma) \text{ with } \lambda = 0 \text{ at } \forall \mathbf{x} \in l_v \end{cases}, \text{ such that} \\ & \int_{\Gamma} \rho (\mathbf{u} \cdot \nabla_{\Gamma}) \mathbf{u} \cdot \tilde{\mathbf{u}} + \frac{\mu}{2} (\nabla_{\Gamma} \mathbf{u} + \nabla_{\Gamma} \mathbf{u}^T) : (\nabla_{\Gamma} \tilde{\mathbf{u}} + \nabla_{\Gamma} \tilde{\mathbf{u}}^T) - p \operatorname{div}_{\Gamma} \tilde{\mathbf{u}} + \mathbf{u} \cdot \nabla_{\Gamma} \tilde{p} \\ & - \mathbf{b}_{\Gamma} \cdot \tilde{\mathbf{u}} + \lambda (\tilde{\mathbf{u}} \cdot \mathbf{n}) + \tilde{\lambda} (\mathbf{u} \cdot \mathbf{n}) \, d\Gamma + \sum_{E \in \mathcal{E}} \int_E -\tau_{BP} \nabla_{\Gamma} p \cdot \nabla_{\Gamma} \tilde{p} \, d\Gamma - \int_{l_v} \mathbf{u}_{l_v} \cdot \mathbf{n}_{\tau} \tilde{p} \, dl \\ & - \int_{\partial\Gamma \setminus l_v} \mathbf{u} \cdot \mathbf{n}_{\tau} \tilde{p} \, dl = 0, \text{ for } \forall \tilde{\mathbf{u}} \in (\mathcal{H}(\Gamma))^3, \forall \tilde{p} \in \mathcal{H}(\Gamma) \text{ and } \forall \tilde{\lambda} \in \mathcal{L}^2(\Gamma), \end{aligned} \quad (31)$$

where the Brezzi-Pitkäranta stabilization term marked in blue color has been imposed on the variational formulation, in order to use the linear elements sketched in Fig. 4 to solve both the fluidic velocity and pressure [69]; \mathcal{E} is an elementization of Γ with $\Gamma = \bigcup_{E \in \mathcal{E}} E$; $\tau_{BP} = h_E^2 / (12\mu)$ is the stabilization parameter with h_E representing the size of the element E .

The distribution of the solute concentration can be solved from the variational formulation of the surface convection-diffusion equation:

$$\begin{aligned} \text{find } & c \in \mathcal{H}(\Gamma) \text{ with } c = c_0 \text{ at } l_v \setminus l_{v0}, \text{ such that} \\ & \int_{\Gamma} (\mathbf{u} \cdot \nabla_{\Gamma} c) \tilde{c} + D \nabla_{\Gamma} c \cdot \nabla_{\Gamma} \tilde{c} \, d\Gamma + \sum_{E \in \mathcal{E}} \int_E \tau_{PG} (\mathbf{u} \cdot \nabla c) (\mathbf{u} \cdot \nabla \tilde{c}) \, d\Gamma = 0, \text{ for } \forall \tilde{c} \in \mathcal{H}(\Gamma), \end{aligned} \quad (32)$$

where the Petrov-Galerkin stabilization term has been imposed on the variational formulation, in order to use the linear elements to solve the concentration [70]; $\tau_{PG} = [4 / (h_E^2 D) + 2 |\mathbf{u}| / h_E]^2$ is the stabilization parameter.

The design destination is to completely mix the fluid with different concentration. The design objective is thus set to minimize the least square measurement of the solute concentration at the open boundary of the surface flow. According to [68], the least square difference measurement is expressed as

$$J = \int_{l_s} (c - \bar{c})^2 \, dl, \quad (33)$$

where \bar{c} is the anticipation of the concentration at the open boundary, and it is the averaged value of the concentration at the boundary with the known non-zero velocity, i.e., $\bar{c} = \int_{l_v \setminus l_{v0}} c_0 \, dl / \int_{l_v \setminus l_{v0}} 1 \, dl$. Based on the adjoint analysis method [60], the variational formulation for the adjoint equation of Eq. 32 can be derived as

$$\begin{aligned} \text{find } & c_a \in \mathcal{H}(\Gamma) \text{ with } c_a = 0 \text{ at } l_v \setminus l_{v0}, \text{ such that} \\ & \int_{\Gamma} 2(c - \bar{c}) \tilde{c}_a + (\mathbf{u} \cdot \nabla_{\Gamma} \tilde{c}_a) c_a + D \nabla_{\Gamma} c_a \cdot \nabla_{\Gamma} \tilde{c}_a \, d\Gamma \\ & + \sum_{E \in \mathcal{E}} \int_E \tau_{PG} (\mathbf{u} \cdot \nabla c_a) (\mathbf{u} \cdot \nabla \tilde{c}_a) \, d\Gamma = 0, \text{ for } \forall \tilde{c}_a \in \mathcal{H}(\Gamma), \end{aligned} \quad (34)$$

where c_a is the adjoint variable of c . Similarly, the variational formulation for the adjoint equation of Eq. 31 can be derived as

$$\begin{aligned} \text{find } & \begin{cases} \mathbf{u}_a \in (\mathcal{H}(\Gamma))^3 \text{ with } \mathbf{u}_a - (\mathbf{u}_a \cdot \mathbf{n}_{\tau}) \mathbf{n}_{\tau} = \mathbf{0} \text{ at } \forall \mathbf{x} \in l_v \\ p_a \in \mathcal{H}(\Gamma) \\ \lambda_a \in \mathcal{L}^2(\Gamma) \text{ with } \lambda_a = 0 \text{ at } \forall \mathbf{x} \in l_v \end{cases}, \text{ such that} \\ & \int_{\Gamma} \rho [(\tilde{\mathbf{u}}_a \cdot \nabla_{\Gamma}) \mathbf{u} \cdot \mathbf{u}_a + (\mathbf{u} \cdot \nabla_{\Gamma}) \tilde{\mathbf{u}}_a \cdot \mathbf{u}_a] + \frac{\mu}{2} (\nabla_{\Gamma} \mathbf{u}_a + \nabla_{\Gamma} \mathbf{u}_a^T) : (\nabla_{\Gamma} \tilde{\mathbf{u}}_a + \nabla_{\Gamma} \tilde{\mathbf{u}}_a^T) \\ & - \tilde{p}_a \operatorname{div}_{\Gamma} \mathbf{u}_a + \tilde{\mathbf{u}}_a \cdot \nabla_{\Gamma} p_a - \frac{\partial \mathbf{b}_{\Gamma}}{\partial \mathbf{u}} \mathbf{u}_a \cdot \tilde{\mathbf{u}}_a + \tilde{\lambda}_a (\mathbf{u}_a \cdot \mathbf{n}) + \lambda_a (\tilde{\mathbf{u}}_a \cdot \mathbf{n}) + (\tilde{\mathbf{u}}_a \cdot \nabla_{\Gamma} c) c_a \, d\Gamma \\ & + \sum_{E \in \mathcal{E}} \int_E -\tau_{BP} \nabla_{\Gamma} p_a \cdot \nabla_{\Gamma} \tilde{p}_a + \tau_{PG} (\tilde{\mathbf{u}}_a \cdot \nabla c) (\mathbf{u} \cdot \nabla c_a) + \tau_{PG} (\mathbf{u} \cdot \nabla c) (\tilde{\mathbf{u}}_a \cdot \nabla c_a) \\ & + \left(\frac{\partial \tau_{PG}}{\partial \mathbf{u}} \cdot \tilde{\mathbf{u}}_a \right) (\mathbf{u} \cdot \nabla c) (\mathbf{u} \cdot \nabla c_a) \, d\Gamma - \int_{\partial\Gamma \setminus l_v} \tilde{\mathbf{u}}_a \cdot \mathbf{n}_{\tau} p_a \, dl = 0, \\ & \text{for } \forall \tilde{\mathbf{u}}_a \in (\mathcal{H}(\Gamma))^3, \forall \tilde{p}_a \in \mathcal{H}(\Gamma) \text{ and } \forall \tilde{\lambda}_a \in \mathcal{L}^2(\Gamma). \end{aligned} \quad (35)$$

Based on the solution of the adjoint variables in Eqs. 34 and 35, the adjoint sensitivity of the design objective in Eq. 33 can be derived.

In order to control the patency of the surface structures used to mix the fluid with different solute concentration, a constraint of the pressure drop instead of the volume fraction is added to the topology optimization problem, where the pressure drop is computed between the known-velocity and open boundaries. The constraint of the pressure drop is expressed as

$$|\Delta P / \Delta P_0 - 1| \leq 10^{-3} \quad \text{with} \quad \Delta P = \int_{l_v \setminus l_{v0}} p \, dl - \int_{l_s} p \, dl \quad (36)$$

where ΔP is the pressure drop; ΔP_0 is a specified value of the desired pressure drop. For the pressure drop ΔP , the variational formulation of the adjoint equation of Eq. 31 is derived as

$$\begin{aligned} \text{find} \quad & \begin{cases} \mathbf{u}_a \in (\mathcal{H}(\Gamma))^3 \text{ with } \mathbf{u}_a - (\mathbf{u}_a \cdot \mathbf{n}_\tau) \mathbf{n}_\tau = \mathbf{0} \text{ at } \forall \mathbf{x} \in l_v \\ p_a \in \mathcal{H}(\Gamma) \\ \lambda_a \in \mathcal{L}^2(\Gamma) \text{ with } \lambda_a = 0 \text{ at } \forall \mathbf{x} \in l_v \end{cases}, \text{ such that} \\ & \int_{\Gamma} \rho [(\tilde{\mathbf{u}}_a \cdot \nabla_{\Gamma}) \mathbf{u} \cdot \mathbf{u}_a + (\mathbf{u} \cdot \nabla_{\Gamma}) \tilde{\mathbf{u}}_a \cdot \mathbf{u}_a] + \frac{\mu}{2} (\nabla_{\Gamma} \mathbf{u}_a + \nabla_{\Gamma} \mathbf{u}_a^T) : (\nabla_{\Gamma} \tilde{\mathbf{u}}_a + \nabla_{\Gamma} \tilde{\mathbf{u}}_a^T) \\ & - \tilde{p}_a \operatorname{div}_{\Gamma} \mathbf{u}_a + \tilde{\mathbf{u}}_a \cdot \nabla_{\Gamma} p_a - \frac{\partial \mathbf{b}_{\Gamma}}{\partial \mathbf{u}} \mathbf{u}_a \cdot \tilde{\mathbf{u}}_a + \tilde{\lambda}_a (\mathbf{u}_a \cdot \mathbf{n}) + \lambda_a (\tilde{\mathbf{u}}_a \cdot \mathbf{n}) + (\tilde{\mathbf{u}}_a \cdot \nabla_{\Gamma} c) c_a \, d\Gamma \\ & + \sum_{E \in \mathcal{E}} \int_E -\tau_{BP} \nabla_{\Gamma} p_a \cdot \nabla_{\Gamma} \tilde{p}_a \, d\Gamma - \int_{\partial \Gamma \setminus l_v} \tilde{\mathbf{u}}_a \cdot \mathbf{n}_{\tau} p_a \, dl + \int_{l_v \setminus l_{v0}} \tilde{p}_a \, dl - \int_{l_s} \tilde{p}_a \, dl = 0, \\ & \text{for } \forall \tilde{\mathbf{u}}_a \in (\mathcal{H}(\Gamma))^3, \forall \tilde{p}_a \in \mathcal{H}(\Gamma) \text{ and } \forall \tilde{\lambda}_a \in \mathcal{L}^2(\Gamma). \end{aligned} \quad (37)$$

Based on the solution of the adjoint variable in Eq. 37, the adjoint sensitivity of the pressure drop can be derived.

Topology optimization of the surface structures for convection-diffusion problems is implemented on the 2-manifolds sketched in Fig. 13, where the known velocity at the inlets is set to be the same as that in Fig. 5. The known distribution of the concentration at the inlets is set to be $c = 2$ and $c = 0$ at the upper and lower half parts of the inlet curves, respectively. The anticipation of the concentration at the open boundary is $\bar{c} = 1$. By setting the diffusion coefficient to be $D = 5 \times 10^{-3}$ and the specified value of the pressure drop to be $\Delta P_0 = 1.5 \times 10^3$, the optimized surface structures, the patterns together with the distributions of the velocity vectors and the corresponding distributions of the solute concentration are derived as shown in Figs. 14(a1-d1), 14(a2-d2) and 14(a3-d3), respectively. The distributions of the velocity vectors show that the mixing length and convection of the surface flows have been enhanced effectively. From the derived results, we can conclude that the roll and bent operation of a 2-manifold can result in different geometrical configuration of the surface structures optimized to control the convection and diffusion in the surface flows. The distributions of the solute concentration on the 2-manifolds without optimized surface structures have been provided in Figs. 14(a4-d4). The values of the design objective corresponding to the distributions of the solute concentration in Figs. 14(a3-d3) and 14(a4-d4) have been listed in Table 4, from which the improved performance achieved by the optimized surface structures can be confirmed.

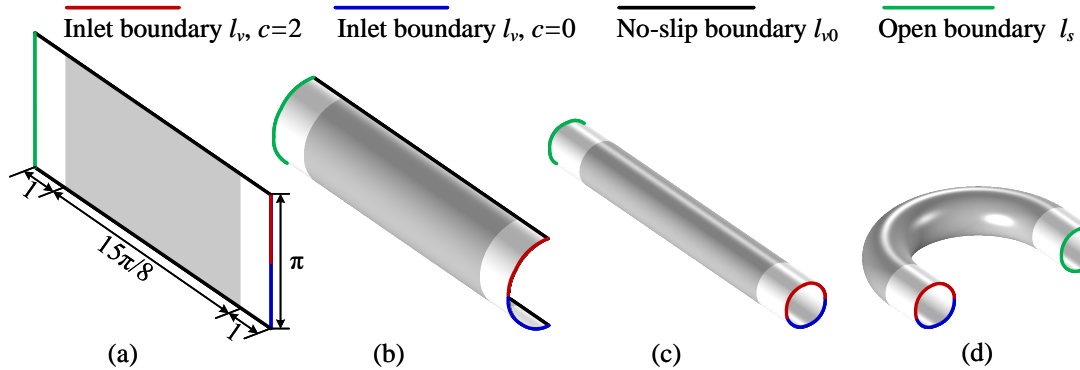


Figure 13: 2-manifolds used in topology optimization of the surface structures for the convection-diffusion problems. The areas of the 2-manifolds are kept to be constant during the deformation. The design domains are colored in gray. The surface channels connected on the design domains are marked in white color. The known velocity at the inlets is set to be parabolic distributions which are the same as that in Fig. 3.

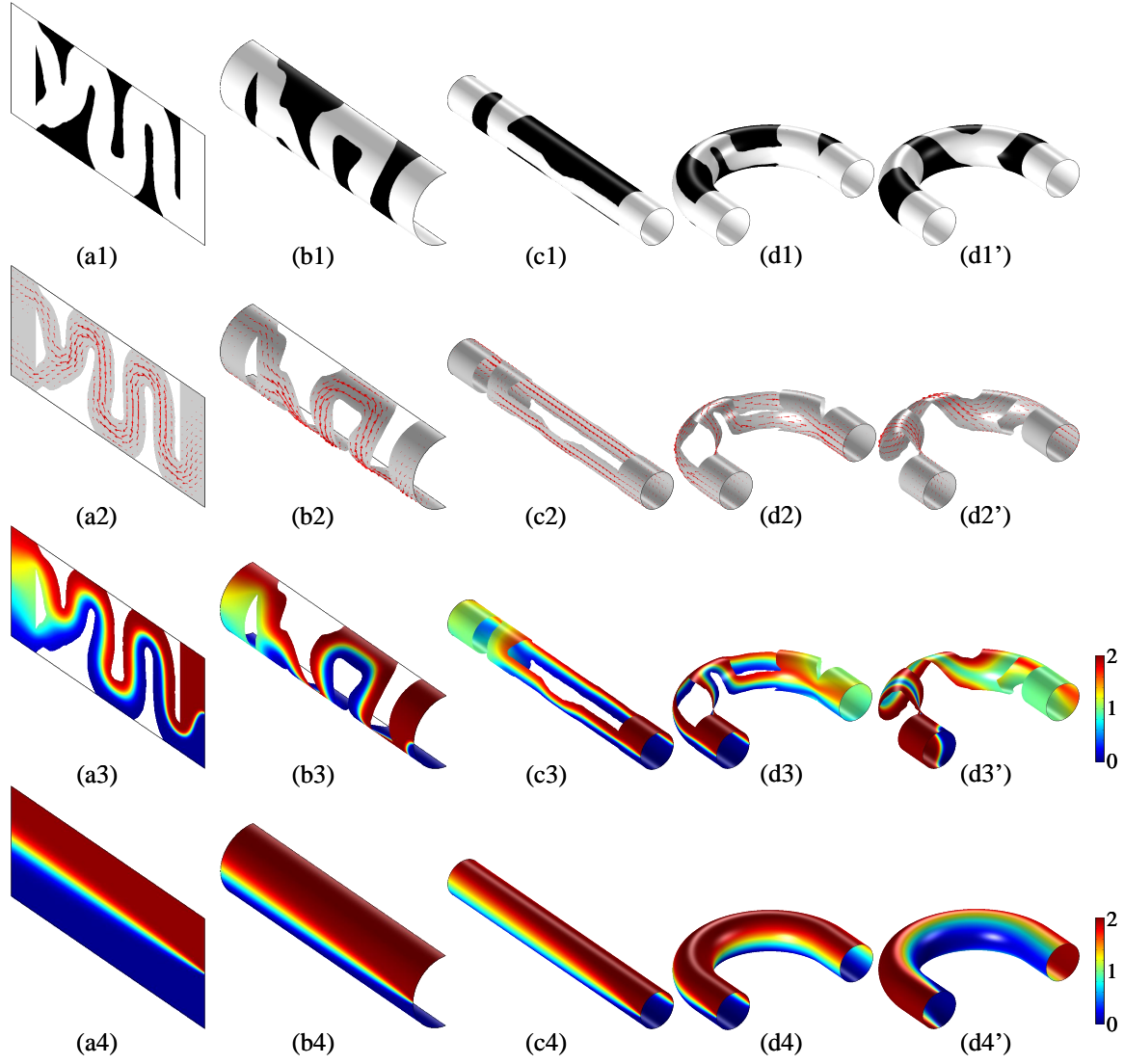


Figure 14: (a1-d1) Optimized surface structures for the convection-diffusion problems derived on the 2-manifolds sketched in Fig. 13. (a2-d2) Patterns of the surface flows corresponding to the derived surface structures, where the distributions of the velocity vectors are presented by the arrows marked in red color. (a3-d3) Distributions of the solute concentration on the patterns of the surface flows. (a4-d4) Distributions of the solute concentration on the 2-manifolds without optimized surface structures. (d1'-d4') Results derived by setting the known distribution of the concentration at the inlets to be $c = 2$ and $c = 0$ at the left and right half parts of the inlet curves, respectively.

	Fig. 14(a3)		Fig. 14(a4)
Eq. 33	0.994	<	2.472
	Fig. 14(b3)		Fig. 14(b4)
Eq. 33	1.049	<	2.473
	Fig. 14(c3)		Fig. 14(c4)
Eq. 33	0.299	<	1.592
	Fig. 14(d3)		Fig. 14(d4)
Eq. 33	0.279	<	1.616
	Fig. 14(d3')		Fig. 14(d4')
Eq. 33	0.206	<	1.606

Table 4: Values of the design objective in Eq. 33 corresponding to the distributions of the solute concentration in Figs. 14(a3-d3') and (a4-d4'). The optimized entries have been noted in bold.

To further confirm the optimized performance of the structures derived for the convection-diffusion problems, the values of the design objective corresponding to the results in Figs. 14(d1-d4) and 14(d1'-d4') are cross compared as listed in Table 5, where the results in Figs. 14(d1'-d4') are derived by setting the known distribution of the solute concentration to be $c = 2$ and $c = 0$ at the left and right half parts of the inlet curves, respectively. From Table 5, the optimized performance of the derived surface structures in Figs. 14(d1-d4) and 14(d1'-d4') can be confirmed from their smaller converged values of the least square difference measurement.

	Fig. 14(d1-d4)		Fig. 14(d1'-d4')
Upper-Lower	0.279	<	0.398
Left-Right	0.431	>	0.206

Table 5: Values of the design objective in Eq. 33 for the surface structures in Figs. 14(d1-d4) and 14(d1'-d4'). 'Upper-Lower' corresponds to the known distribution of the concentration at the inlet set to be $c = 2$ and $c = 0$ at the upper and lower half parts of the inlet curves, respectively; 'Left-Right' corresponds to the known distribution of the solute concentration set to be $c = 2$ and $c = 0$ at the left and right half parts of the inlet curves, respectively. The optimized entries have been noted in bold.

5 Conclusions

This paper has developed a topology optimization approach for the surface flows at the solid/liquid or liquid/vapor interfaces, where the fluidic motion is described by the surface Navier-Stokes equations defined on 2-manifolds. This approach is implemented by filling a porous medium onto the design domains in the form of 2-manifolds, where an artificial Darcy friction force is added to the surface Navier-Stokes equations. When an area force induced by an exterior physical field is imposed on the surface flows, it is penalized to avoid the invalidity of the porous medium model of this topology optimization approach, by eliminating its existence in the solid phase.

The outlined topology optimization approach has been implemented for steady and unsteady surface flows, respectively. For the steady surface flows, this approach has been carried out for the surface flows driven by boundary velocity on a series of 2-manifolds deformed from the ones with boundaries to the ones without boundaries. For the unsteady surface flows, this approach has been performed for the surface flows driven by the area forces induced by rotations around fixed axes, where a time dependent angular velocity is imposed; along with the time dependent rotations, the centrifugal, Coriolis and Euler forces are generated and loaded on the surface flows. The derived numerical results can provide intuitive understanding of the optimized topology on the continuously deformed 2-manifolds and the actuation performance of area forces for the surface flows. This approach has been extended to implement topology optimization for the convection-diffusion problems defined on 2-manifolds, where the Brezzi-Pitkäranta stabilization has been introduced to solve the surface Navier-Stokes equations by using the linear surface elements.

This topology optimization approach can provide an optimization based inverse design method for the surface structures of aerocrafts and submarines, for which the outer shape can be described as static 2-manifolds and the fluidic velocity is tangential to the solid/fluid interface with approximated complete slip property. In the future, we will implement topology optimization for the surface flows including the evolution of 2-manifolds caused by the normal velocity of the surface flows. This is significant to include more dynamic effects into the topology optimization for fluid mechanics.

6 Acknowledgements

The authors are grateful to Prof. K. Svanberg of KTH for supplying the MMA codes. Y. Deng, W. Zhang, J. Zhu and J. Bai acknowledge the support from the National Natural Science Foundation of China (Nos. 51875545, 11722219, 11620101002); Y. Deng acknowledges a Humboldt Research Fellowship for Experienced Researchers (Humboldt-ID: 1197305); W. Zhang and J. Zhu acknowledge the support from the National Key Research and Development Program (No. 2017YFB1102800); Z. Liu acknowledges the support from the National Natural Science Foundation of China (No. 51675506); J.G. Korvink acknowledges the support from an EU2020 FET grant (TiSuMR, 737043), the DFG under grant KO 1883/20-1 Metacoils, funding within the framework of the German Excellence Initiative under grant EXC 2082 "3D Matter Made to Order", and from the VirtMat initiative "Virtual Materials Design".

7 Appendix

This section provides the details for the surface finite element solutions of the variational formulations of the PDEs in Section 2.

7.1 Surface finite element solution

To solve the variational formulations of the PDEs and their adjoint equations, a surface finite element method is utilized [61]. In the surface finite element method, the 2-manifold Γ is approximated by a discrete surface denoted by $\Gamma_h = \bigcup_{E \in \mathcal{E}_h} E$, where E is a finite element and \mathcal{E}_h is the elementization of Γ sketched in Fig. 15. The quadrangular and triangular elements are usually used to discretize a 2-manifold. In this paper, quadrangular elements are used.

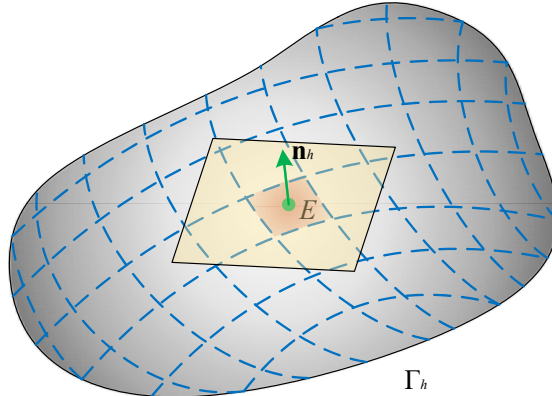


Figure 15: Sketch for the elementization of Γ by using quadrangular elements, where Γ_h is the discrete surface, E is a quadrangular element and \mathbf{n}_h is the unitary normal vector on Γ_h .

Taylor-Hood elements are used to satisfy the inf-sup condition to ensure the well-posedness of the variational formulations of the surface Navier-Stokes equations and their adjoint equations [63]. Linear elements are used to interpolate and solve the variational formulations of the surface-PDE filter and its adjoint equation, to ensure the positivity of the design variable. The finite element nodes of a Taylor-Hood element and a linear element of the elementization \mathcal{E}_h have been sketched in Fig. 4. Quadratic elements are used for the fluidic velocity \mathbf{u} , Lagrangian multiplier λ and their adjoint variables. The corresponding finite element space is

$$\mathcal{S}_h^{(2)} = \{ \phi_h \in \mathcal{C}^0(\Gamma_h) : \phi_h(\mathbf{x})|_{\mathbf{x} \in E, \forall E \in \mathcal{E}_h} \text{ is a quadratic affine} \}, \quad (38)$$

where $\mathcal{C}^0(\Gamma_h)$ defined on Γ_h is a space of the continuous functions with compact support. This space can be spanned by the nodal basis $\{ \psi_1^{(2)}, \psi_2^{(2)}, \dots, \psi_{N_2}^{(2)} \}$ satisfying

$$\left. \begin{array}{l} \psi_i^{(2)} \in \mathcal{S}_h^{(2)} \\ \psi_i^{(2)}(\mathbf{x}_j^{(2)}) = \delta_{ij} \end{array} \right\} \text{ for } i, j = 1, 2, \dots, N_2 \quad (39)$$

where N_2 is the number of interpolation nodes; $\{ \mathbf{x}_j^{(2)} : j = 1, 2, \dots, N_2 \} \subset \Gamma$ denotes the nodes for quadratic interpolation on the elementization \mathcal{E}_h ; δ_{ij} is the Kronecker symbol. δ_{ij} is 1 when $i = j$ is satisfied; or else, it is 0. Linear elements are used for the fluidic pressure p , the design variable γ , the filtered design variable γ_f and their adjoint variables. The corresponding finite element space is

$$\mathcal{S}_h^{(1)} = \{ \phi_h \in \mathcal{C}^0(\Gamma_h) : \phi_h(\mathbf{x})|_{\mathbf{x} \in E, \forall E \in \mathcal{E}_h} \text{ is a bilinear affine} \}. \quad (40)$$

This space can be spanned by the nodal basis $\{ \psi_1^{(1)}, \psi_2^{(1)}, \dots, \psi_{N_1}^{(1)} \}$ satisfying

$$\left. \begin{array}{l} \psi_i^{(1)} \in \mathcal{S}_h^{(1)} \\ \psi_i^{(1)}(\mathbf{x}_j^{(1)}) = \delta_{ij} \end{array} \right\} \text{ for } i, j = 1, 2, \dots, N_1 \quad (41)$$

where N_1 is the number of the interpolation nodes; $\{ \mathbf{x}_j^{(1)} : j = 1, 2, \dots, N_1 \} \subset \Gamma$ denotes the nodes for the bilinear interpolation on the elementization \mathcal{E}_h .

To discretize the time derivative terms of the variational formulations, the backward differentiation formula (BDF) is utilized [62]. The forms of the m -step BDF are provided for the cases of $m \leq 6$ with m representing the step number of the BDF algorithm, because the methods with $m > 6$ are not zero-stable [65].

7.1.1 Discretization of variational formulation in Eq. 13

Based on the surface finite element method, the variational formulation in Eq. 13 for the surface-PDE filter can be discretized into the following formulation defined on Γ_h :

$$\begin{aligned} & \text{find } \gamma_{f,h} \in \mathcal{S}_h^{(1)}, \text{ such that} \\ & \int_{\Gamma_h} r_f^2 \nabla_{\Gamma_h} \gamma_{f,h} \cdot \nabla_{\Gamma_h} \tilde{\gamma}_{f,h} + \gamma_{f,h} \tilde{\gamma}_{f,h} - \gamma_h \tilde{\gamma}_{f,h} \, d\Gamma = 0 \text{ for } \forall \tilde{\gamma}_{f,h} \in \mathcal{S}_h^{(1)}, \end{aligned} \quad (42)$$

where γ_h and $\gamma_{f,h}$ are the design variable and its filtered counterpart on Γ_h ; $\nabla_{\Gamma_h} v = \mathbf{P}_h \nabla v$ is the tangential gradient of a scalar function $v : \Gamma_h \mapsto \mathbb{R}$, with ∇ representing the spatial gradient operator, $\mathbf{P}_h = \mathbf{I} - \mathbf{n}_h \mathbf{n}_h^T$ representing the normal projector on the tangential space of Γ_h and \mathbf{n}_h denoting the unitary normal vector on Γ_h sketched in Fig. 15.

Based on the nodal basis $\{\psi_1^{(1)}, \psi_2^{(1)}, \dots, \psi_{N_1}^{(1)}\}$ of $\mathcal{S}_h^{(1)}$, γ_h and $\gamma_{f,h}$ can be expressed as:

$$\left. \begin{aligned} \gamma_h &= \sum_{i=1}^{N_1} \Upsilon_{h,i} \psi_i^{(1)}(\mathbf{x}) \\ \gamma_{f,h} &= \sum_{i=1}^{N_1} \Upsilon_{f,h,i} \psi_i^{(1)}(\mathbf{x}) \end{aligned} \right\} \text{ at } \forall \mathbf{x} \in \Gamma_h, \quad (43)$$

where $\Upsilon_{h,i}$ and $\Upsilon_{f,h,i}$ are the nodal variables of γ_h and $\gamma_{f,h}$, respectively. By substituting Eq. 43 into Eq. 42 and using the nodal basis of $\mathcal{S}_h^{(1)}$ as the test functions, a linear system can be derived based on the assembly rule of stiffness matrix:

$$(\mathbf{K} + \mathbf{N}) \Upsilon_f = \mathbf{N} \Upsilon, \quad (44)$$

where Υ_f and Υ are the discrete counterparts of $\gamma_{f,h}$ and γ_h , respectively. The correspondences between the matrixes in Eq. 44 and terms in Eq. 43 are provided by Eq. 69 in Section 7.1.7. The variational formulation in Eq. 13 can be solved by using a PARDISO solver [66].

7.1.2 Discretization of variational formulation in Eq. 9

Based on the surface finite element method and m -step BDF schemes, the variational formulation in Eq. 9 for the surface Navier-Stokes equations can be discretized into the following formulation defined on Γ_h :

for $n = 1, 2, \dots, N_t$

$$\text{find } \begin{cases} \mathbf{u}_h^{(n)} \in (\mathcal{S}_h^{(2)})^3 \text{ with } \begin{cases} \mathbf{u}_h^{(n)} - (\mathbf{u}_h^{(n)} \cdot \mathbf{n}_{\tau,h}) \mathbf{n}_{\tau,h} = \mathbf{u}_{l_v} - (\mathbf{u}_{l_v} \cdot \mathbf{n}_{\tau,h}) \mathbf{n}_{\tau,h} \text{ at } t = n\Delta t, \forall \mathbf{x} \in l_{v,h}, \\ \mathbf{u}_h^{(0)} = \mathbf{u}_0 \text{ at } \forall \mathbf{x} \in \Gamma_h \end{cases} \\ p_h^{(n)} \in \mathcal{S}_h^{(1)} \text{ with } p_h^{(n)} = p_0 \text{ at } t = n\Delta t, \forall \mathbf{x} \in \mathcal{P}_h, \\ \lambda_h^{(n)} \in \mathcal{S}_h^{(2)} \text{ with } \lambda_h^{(n)} = 0 \text{ at } t = n\Delta t, \forall \mathbf{x} \in l_{v,h}, \end{cases},$$

$$\begin{aligned} & \text{such that } \int_{\Gamma_h} \rho \frac{\theta_m \mathbf{u}_h^{(n)} - \mathbf{u}_{h,m}^{(n-1)}}{\Delta t} \cdot \tilde{\mathbf{u}}_h + \rho \left[(\mathbf{u}_h^{(n)} \cdot \nabla_{\Gamma_h}) \mathbf{u}_h^{(n)} \right] \cdot \tilde{\mathbf{u}}_h \\ & + \frac{\mu}{2} (\nabla_{\Gamma_h} \mathbf{u}_h^{(n)} + \nabla_{\Gamma_h} \mathbf{u}_h^{(n)T}) : (\nabla_{\Gamma_h} \tilde{\mathbf{u}}_h + \nabla_{\Gamma_h} \tilde{\mathbf{u}}_h^T) - p_h^{(n)} \text{div}_{\Gamma_h} \tilde{\mathbf{u}}_h + \mathbf{u}_h^{(n)} \cdot \nabla_{\Gamma_h} \tilde{p}_h \\ & + (\alpha_h \mathbf{u}_h^{(n)} - \chi_h \mathbf{b}_{p,h}^{(n)}) \cdot \tilde{\mathbf{u}}_h + \lambda_h^{(n)} (\tilde{\mathbf{u}}_h \cdot \mathbf{n}_h) + \tilde{\lambda}_h (\mathbf{u}_h^{(n)} \cdot \mathbf{n}_h) \, d\Gamma - \int_{l_{v,h}} \mathbf{u}_{l_v} \cdot \mathbf{n}_{\tau,h} \tilde{p}_h \, dl \\ & - \int_{\partial\Gamma_h \setminus l_{v,h}} \mathbf{u}_h^{(n)} \cdot \mathbf{n}_{\tau,h} \tilde{p}_h \, dl = 0, \text{ for } \forall \tilde{\mathbf{u}}_h \in (\mathcal{S}_h^{(2)})^3, \forall \tilde{p}_h \in \mathcal{S}_h^{(1)} \text{ and } \tilde{\lambda}_h \in \mathcal{S}_h^{(2)}, \end{aligned} \quad (45)$$

where $\text{div}_{\Gamma_h} \mathbf{v} = \text{tr}((\nabla \mathbf{v}) \mathbf{P}_h)$ is the divergence of a vector function $\mathbf{v} : \Gamma_h \mapsto \mathbb{R}^3$; n is the time step number, and it is used as the superscript of the relevant variables and functions to denote the time step; the time domain $(0, T)$ is divided into N_t sections with the time-step length of $\Delta t = T/N_t$, respectively; the time-step number N_t is chosen to be large enough to ensure the numerical stability and accuracy; $\mathbf{u}_h^{(n)}$, $p_h^{(n)}$ and $\lambda_h^{(n)}$ are the fluidic velocity, the pressure and the Lagrangian multiplier on Γ_h at time $t = n\Delta t$, respectively; $\tilde{\mathbf{u}}_h$, \tilde{p}_h and $\tilde{\lambda}_h$ are the test functions of $\mathbf{u}_h^{(n)}$, $p_h^{(n)}$ and $\lambda_h^{(n)}$, respectively; α_h and χ_h are the impermeability and the penalization factor on Γ_h , respectively; $l_{v,h}$ and \mathcal{P}_h are the discrete counterparts of l_v and \mathcal{P} , respectively; for the m -step BDF schemes, the values of the parameter θ_m and the expression of $\mathbf{u}_{h,m}^{(n-1)}$ determined by the linear combination of $\{\mathbf{u}_h^{(n-1)}, \mathbf{u}_h^{(n-2)}, \dots, \mathbf{u}_h^{(n-m)}\}$ are provided in Tables 6 and 7.

m	θ_m
1	1
2	3/2
3	11/6
4	25/12
5	137/60
6	147/60

Table 6: Values of the parameter θ_m for the m -step BDF schemes.

n, m	$\mathbf{u}_{h,m}^{(n-1)}$
$n \geq 1, m = 1$	$\mathbf{u}_h^{(n-1)}$
$n \geq 2, m \leq 2$	$2\mathbf{u}_h^{(n-1)} - \frac{1}{2}\mathbf{u}_h^{(n-2)}$
$n \geq 3, m \leq 3$	$3\mathbf{u}_h^{(n-1)} - \frac{3}{2}\mathbf{u}_h^{(n-2)} + \frac{1}{3}\mathbf{u}_h^{(n-3)}$
$n \geq 4, m \leq 4$	$4\mathbf{u}_h^{(n-1)} - 3\mathbf{u}_h^{(n-2)} + \frac{4}{3}\mathbf{u}_h^{(n-3)} - \frac{1}{4}\mathbf{u}_h^{(n-4)}$
$n \geq 5, m \leq 5$	$5\mathbf{u}_h^{(n-1)} - 5\mathbf{u}_h^{(n-2)} + \frac{10}{3}\mathbf{u}_h^{(n-3)} - \frac{5}{4}\mathbf{u}_h^{(n-4)} + \frac{1}{5}\mathbf{u}_h^{(n-5)}$
$n \geq 6, m \leq 6$	$6\mathbf{u}_h^{(n-1)} - \frac{15}{2}\mathbf{u}_h^{(n-2)} + \frac{20}{3}\mathbf{u}_h^{(n-3)} - \frac{15}{4}\mathbf{u}_h^{(n-4)} + \frac{6}{5}\mathbf{u}_h^{(n-5)} - \frac{1}{6}\mathbf{u}_h^{(n-6)}$

Table 7: Expressions of $\mathbf{u}_{h,m}^{(n-1)}$ for the m -step BDF schemes, where $\mathbf{u}_h^{(n-1)}$ is the initial distribution of the fluidic velocity \mathbf{u}_0 for $n = 1$.

The discretized variational formulation of the surface Navier-Stokes equations in Eq. 45 is nonlinear because of the convection term $\rho [(\mathbf{u}_h^{(n)} \cdot \nabla_{\Gamma_h}) \mathbf{u}_h^{(n)}] \cdot \tilde{\mathbf{u}}_h$. Newton iteration turns out to be a natural approach to solve it based on the perturbation-based linearization [63]. Given the iterate $(\mathbf{u}_{h,k}^{(n)}, p_{h,k}^{(n)}, \lambda_{h,k}^{(n)})$ with the subscript k representing the iteration number of the Newton iteration, the computation can be started from the residuals associated with the variational formulation in Eq. 45. In the Newton iteration, the corrections $\{\delta \mathbf{u}_{h,k}^{(n)} \in (\mathcal{S}_h^{(2)})^3, \delta p_{h,k}^{(n)} \in \mathcal{S}_h^{(1)}, \delta \lambda_{h,k}^{(n)} \in \mathcal{S}_h^{(2)}\}$ for $\{\mathbf{u}_h^{(n)} = \mathbf{u}_{h,k}^{(n)} + \delta \mathbf{u}_{h,k}^{(n)}, p_h^{(n)} = p_{h,k}^{(n)} + \delta p_{h,k}^{(n)}, \lambda_h^{(n)} = \lambda_{h,k}^{(n)} + \delta \lambda_{h,k}^{(n)}\}$ satisfy

$$\begin{aligned}
& \int_{\Gamma_h} \rho \frac{\theta_m}{\Delta t} \delta \mathbf{u}_{h,k}^{(n)} \cdot \tilde{\mathbf{u}}_h + \rho [(\mathbf{u}_{h,k}^{(n)} \cdot \nabla_{\Gamma_h}) \delta \mathbf{u}_{h,k}^{(n)}] \cdot \tilde{\mathbf{u}}_h + \rho [(\delta \mathbf{u}_{h,k}^{(n)} \cdot \nabla_{\Gamma_h}) \mathbf{u}_{h,k}^{(n)}] \cdot \tilde{\mathbf{u}}_h \\
& + \frac{\mu}{2} (\nabla_{\Gamma_h} \delta \mathbf{u}_{h,k}^{(n)} + \nabla_{\Gamma_h} \delta \mathbf{u}_{h,k}^{(n)\top}) : (\nabla_{\Gamma_h} \tilde{\mathbf{u}}_h + \nabla_{\Gamma_h} \tilde{\mathbf{u}}_h^\top) \\
& - \delta p_{h,k}^{(n)} \operatorname{div}_{\Gamma_h} \tilde{\mathbf{u}}_h + \delta \mathbf{u}_{h,k}^{(n)} \cdot \nabla_{\Gamma_h} \tilde{p}_h + \left(\alpha_h \delta \mathbf{u}_{h,k}^{(n)} - \chi_h \frac{\partial \mathbf{b}_{p,h}^{(n)}}{\partial \mathbf{u}_{h,k}^{(n)}} \delta \mathbf{u}_{h,k}^{(n)} \right) \cdot \tilde{\mathbf{u}}_h \\
& + \delta \lambda_{h,k}^{(n)} (\tilde{\mathbf{u}}_h \cdot \mathbf{n}_h) + \tilde{\lambda}_h (\delta \mathbf{u}_{h,k}^{(n)} \cdot \mathbf{n}_h) \, d\Gamma - \int_{\partial \Gamma_h \setminus l_{v,h}} \delta \mathbf{u}_{h,k}^{(n)} \cdot \mathbf{n}_{\tau,h} \tilde{p}_h \, dl \\
& = - \int_{\Gamma_h} \rho \frac{\theta_m \mathbf{u}_{h,k}^{(n)} - \mathbf{u}_{h,m}^{(n-1)}}{\Delta t} \cdot \tilde{\mathbf{u}}_h + \rho [(\mathbf{u}_{h,k}^{(n)} \cdot \nabla_{\Gamma_h}) \mathbf{u}_{h,k}^{(n)}] \cdot \tilde{\mathbf{u}}_h \\
& + \frac{\mu}{2} (\nabla_{\Gamma_h} \mathbf{u}_{h,k}^{(n)} + \nabla_{\Gamma_h} \mathbf{u}_{h,k}^{(n)\top}) : (\nabla_{\Gamma_h} \tilde{\mathbf{u}}_h + \nabla_{\Gamma_h} \tilde{\mathbf{u}}_h^\top) - p_{h,k}^{(n)} \operatorname{div}_{\Gamma_h} \tilde{\mathbf{u}}_h \\
& + \mathbf{u}_{h,k}^{(n)} \cdot \nabla_{\Gamma_h} \tilde{p}_h + \left(\alpha_h \mathbf{u}_{h,k}^{(n)} - \chi_h \mathbf{b}_{p,h}^{(n)}(\mathbf{u}_{h,k}^{(n)}) \right) \cdot \tilde{\mathbf{u}}_h + \lambda_{h,k}^{(n)} (\tilde{\mathbf{u}}_h \cdot \mathbf{n}_h) \\
& + \tilde{\lambda}_h (\mathbf{u}_{h,k}^{(n)} \cdot \mathbf{n}_h) \, d\Gamma + \int_{l_{v,h}} \mathbf{u}_{l_v} \cdot \mathbf{n}_{\tau,h} \tilde{p}_h \, dl + \int_{\partial \Gamma_h \setminus l_{v,h}} \mathbf{u}_{h,k}^{(n)} \cdot \mathbf{n}_{\tau,h} \tilde{p}_h \, dl.
\end{aligned} \tag{46}$$

By setting

$$\left\{ \begin{array}{l} R_{\mathbf{u}_t, k}^{(n)}(\tilde{\mathbf{u}}_h) := - \int_{\Gamma_h} \rho \frac{\theta_m \mathbf{u}_{h,k}^{(n)} - \mathbf{u}_{h,m}^{(n-1)}}{\Delta t} \cdot \tilde{\mathbf{u}}_h \, d\Gamma, \\ R_{\mathbf{u}, k}^{(n)}(\tilde{\mathbf{u}}_h) := - \int_{\Gamma_h} \rho \left[\left(\mathbf{u}_{h,k}^{(n)} \cdot \nabla_{\Gamma_h} \right) \mathbf{u}_{h,k}^{(n)} \right] \cdot \tilde{\mathbf{u}}_h \\ \quad + \frac{\mu}{2} \left(\nabla_{\Gamma_h} \mathbf{u}_{h,k}^{(n)} + \nabla_{\Gamma_h} \mathbf{u}_{h,k}^{(n)\top} \right) : \left(\nabla_{\Gamma_h} \tilde{\mathbf{u}}_h + \nabla_{\Gamma_h} \tilde{\mathbf{u}}_h^\top \right) \\ \quad - p_{h,k}^{(n)} \operatorname{div}_{\Gamma_h} \tilde{\mathbf{u}}_h + \left(\alpha_h \mathbf{u}_{h,k}^{(n)} - \chi_h \mathbf{b}_{p,h}^{(n)} \left(\mathbf{u}_{h,k}^{(n)} \right) \right) \cdot \tilde{\mathbf{u}}_h + \lambda_{h,k}^{(n)} \left(\tilde{\mathbf{u}}_h \cdot \mathbf{n}_h \right) \, d\Gamma, \\ R_{p,k}^{(n)}(\tilde{p}_h) := - \int_{\Gamma_h} \mathbf{u}_{h,k}^{(n)} \cdot \nabla_{\Gamma_h} \tilde{p}_h \, d\Gamma + \int_{l_{v,h}} \mathbf{u}_{l_v} \cdot \mathbf{n}_{\tau,h} \tilde{p}_h \, dl + \int_{\partial\Gamma_h \setminus l_{v,h}} \mathbf{u}_{h,k}^{(n)} \cdot \mathbf{n}_{\tau,h} \tilde{p}_h \, dl, \\ R_{\lambda,k}^{(n)}(\tilde{\lambda}_h) := - \int_{\Gamma_h} \tilde{\lambda}_h \left(\mathbf{u}_{h,k}^{(n)} \cdot \mathbf{n}_h \right) \, d\Gamma, \end{array} \right. \quad (47)$$

Eq. 46 can be equivalently transformed into

$$\left\{ \begin{array}{l} \int_{\Gamma_h} \rho \frac{\theta_m}{\Delta t} \delta \mathbf{u}_{h,k}^{(n)} \cdot \tilde{\mathbf{u}}_h + \rho \left[\left(\mathbf{u}_{h,k}^{(n)} \cdot \nabla_{\Gamma_h} \right) \delta \mathbf{u}_{h,k}^{(n)} \right] \cdot \tilde{\mathbf{u}}_h + \rho \left[\left(\delta \mathbf{u}_{h,k}^{(n)} \cdot \nabla_{\Gamma_h} \right) \mathbf{u}_{h,k}^{(n)} \right] \cdot \tilde{\mathbf{u}}_h \\ \quad + \frac{\mu}{2} \left(\nabla_{\Gamma_h} \delta \mathbf{u}_{h,k}^{(n)} + \nabla_{\Gamma_h} \delta \mathbf{u}_{h,k}^{(n)\top} \right) : \left(\nabla_{\Gamma_h} \tilde{\mathbf{u}}_h + \nabla_{\Gamma_h} \tilde{\mathbf{u}}_h^\top \right) - \delta p_{h,k}^{(n)} \operatorname{div}_{\Gamma_h} \tilde{\mathbf{u}}_h \\ \quad + \left(\alpha_h \delta \mathbf{u}_{h,k}^{(n)} - \chi_h \frac{\partial \mathbf{b}_{p,h}^{(n)}}{\partial \mathbf{u}_{h,k}^{(n)}} \delta \mathbf{u}_{h,k}^{(n)} \right) \cdot \tilde{\mathbf{u}}_h + \delta \lambda_{h,k}^{(n)} \left(\tilde{\mathbf{u}}_h \cdot \mathbf{n}_h \right) \, d\Gamma = R_{\mathbf{u}_t, k}^{(n)}(\tilde{\mathbf{u}}_h) + R_{\mathbf{u}, k}^{(n)}(\tilde{\mathbf{u}}_h), \\ \int_{\Gamma_h} \delta \mathbf{u}_{h,k}^{(n)} \cdot \nabla_{\Gamma_h} \tilde{p}_h \, d\Gamma - \int_{\partial\Gamma_h \setminus l_{v,h}} \delta \mathbf{u}_{h,k}^{(n)} \cdot \mathbf{n}_{\tau,h} \tilde{p}_h \, dl = R_{p,k}^{(n)}(\tilde{p}_h), \\ \int_{\Gamma_h} \tilde{\lambda}_h \left(\delta \mathbf{u}_{h,k}^{(n)} \cdot \mathbf{n}_h \right) \, d\Gamma = R_{\lambda,k}^{(n)}(\tilde{\lambda}_h), \end{array} \right. \quad (48)$$

where $R_{\mathbf{u}, k}^{(n)}(\tilde{\mathbf{u}}_h)$, $R_{p,k}^{(n)}(\tilde{p}_h)$ and $R_{\lambda,k}^{(n)}(\tilde{\lambda}_h)$ are the residuals associated with the variational formulation in Eq. 45.

Based on the nodal basis $\{\psi_1^{(2)}, \psi_2^{(2)}, \dots, \psi_{N_2}^{(2)}\}$ of $\mathcal{S}_h^{(2)}$, $\mathbf{u}_{h,k}^{(n)}$, $\delta \mathbf{u}_{h,k}^{(n)}$, $\lambda_{h,k}^{(n)}$ and $\delta \lambda_{h,k}^{(n)}$ have the following transformations:

$$\left. \begin{array}{l} \mathbf{u}_{h,k}^{(n)} = \sum_{i=1}^{N_2} \mathbf{U}_{k,i}^{(n)} \psi_i^{(2)}(\mathbf{x}) \\ \delta \mathbf{u}_{h,k}^{(n)} = \sum_{i=1}^{N_2} \Delta \mathbf{U}_{k,i}^{(n)} \psi_i^{(2)}(\mathbf{x}) \\ \lambda_{h,k}^{(n)} = \sum_{i=1}^{N_2} \Lambda_{k,i}^{(n)} \psi_i^{(2)}(\mathbf{x}) \\ \delta \lambda_{h,k}^{(n)} = \sum_{i=1}^{N_2} \Delta \Lambda_{k,i}^{(n)} \psi_i^{(2)}(\mathbf{x}) \end{array} \right\} \text{ at } \forall \mathbf{x} \in \Gamma_h, \quad (49)$$

where $\mathbf{U}_{k,i}^{(n)}$, $\Delta \mathbf{U}_{k,i}^{(n)}$, $\Lambda_{k,i}^{(n)}$ and $\Delta \Lambda_{k,i}^{(n)}$ are the nodal variables of $\mathbf{u}_{h,k}^{(n)}$, $\delta \mathbf{u}_{h,k}^{(n)}$, $\lambda_{h,k}^{(n)}$ and $\delta \lambda_{h,k}^{(n)}$, respectively. Based on the nodal basis $\{\psi_1^{(1)}, \psi_2^{(1)}, \dots, \psi_{N_1}^{(1)}\}$ of $\mathcal{S}_h^{(1)}$, $p_{h,k}^{(n)}$ and $\delta p_{h,k}^{(n)}$ have the following transformations:

$$\left. \begin{array}{l} p_{h,k}^{(n)} = \sum_{i=1}^{N_1} P_{k,i}^{(n)} \psi_i^{(1)}(\mathbf{x}) \\ \delta p_{h,k}^{(n)} = \sum_{i=1}^{N_1} \Delta P_{k,i}^{(n)} \psi_i^{(1)}(\mathbf{x}) \end{array} \right\} \text{ at } \forall \mathbf{x} \in \Gamma_h, \quad (50)$$

where $P_{k,i}^{(n)}$ and $\Delta P_{k,i}^{(n)}$ are the nodal variables of $p_{h,k}^{(n)}$ and $\delta p_{h,k}^{(n)}$, respectively. By substituting Eqs. 49 and 50 into Eq. 48, and using the nodal basis of $\mathcal{S}_h^{(2)}$ and $\mathcal{S}_h^{(1)}$ as the test functions, a

linear system can be derived based on the assembly rule of stiffness matrix:

$$\begin{cases} [\mathbf{A} + \mathbf{B}_1(\mathbf{U}_k^{(n)}) + \mathbf{B}_2(\mathbf{U}_k^{(n)}) + \mathbf{C}] \Delta \mathbf{U}_k^{(n)} + \mathbf{D}_1 \Delta \mathbf{P}_k^{(n)} + \mathbf{E}(\boldsymbol{\Upsilon}_p) \Delta \mathbf{U}_k^{(n)} + \\ \mathbf{F} \Delta \boldsymbol{\Lambda}_k^{(n)} = \mathbf{R}_{\mathbf{u}_t, k}^{(n)}(\mathbf{U}_k^{(n)}, \mathbf{U}_k^{(n-1)}, \dots, \mathbf{U}_k^{(n-m)}) + \mathbf{R}_{\mathbf{u}, k}^{(n)}(\mathbf{U}_k^{(n)}, \mathbf{P}_k^{(n)}, \boldsymbol{\Lambda}_k^{(n)}; \boldsymbol{\Upsilon}_p), \\ \mathbf{D}_2^T \Delta \mathbf{U}_k^{(n)} = \mathbf{R}_{p, k}^{(n)}(\mathbf{U}_k^{(n)}), \\ \mathbf{F}^T \Delta \mathbf{U}_k^{(n)} = \mathbf{R}_{\lambda, k}^{(n)}(\mathbf{U}_k^{(n)}), \end{cases} \quad (51)$$

where $\boldsymbol{\Upsilon}_p$ is a column vector corresponding to the discrete counterpart of the physical density γ_p in the current iteration of the topology optimization procedure in Table 1; $\mathbf{R}_{\mathbf{u}_t, k}^{(n)}$ depends on $\{\mathbf{U}_k^{(n-1)}, \mathbf{U}_k^{(n-2)}, \dots, \mathbf{U}_k^{(n-m)}\}$, because $\mathbf{u}_{h, m}^{(n-1)}$ is the linear combination of $\{\mathbf{u}_h^{(n-1)}, \mathbf{u}_h^{(n-2)}, \dots, \mathbf{u}_h^{(n-m)}\}$; $\mathbf{U}_k^{(n)}, \mathbf{P}_k^{(n)}, \boldsymbol{\Lambda}_k^{(n)}, \Delta \mathbf{U}_k^{(n)}, \Delta \mathbf{P}_k^{(n)}$ and $\Delta \boldsymbol{\Lambda}_k^{(n)}$ are the discrete counterparts of $\mathbf{u}_h^{(n)}, p_{h, k}^{(n)}, \lambda_{h, k}^{(n)}, \delta \mathbf{u}_{h, k}^{(n)}, \delta p_{h, k}^{(n)}$ and $\delta \lambda_{h, k}^{(n)}$, respectively; the discrete counterparts of $\mathbf{u}_h^{(n)}, p_h^{(n)}$ and $\lambda_h^{(n)}$ are

$$\begin{cases} \mathbf{U}^{(n)} := \mathbf{U}_k^{(n)} + \Delta \mathbf{U}_k^{(n)}, \\ \mathbf{P}^{(n)} := \mathbf{P}_k^{(n)} + \Delta \mathbf{P}_k^{(n)}, \\ \boldsymbol{\Lambda}^{(n)} := \boldsymbol{\Lambda}_k^{(n)} + \Delta \boldsymbol{\Lambda}_k^{(n)}. \end{cases} \quad (52)$$

The correspondence between the matrixes in Eq. 51 and terms in Eqs. 47 and 48 are provided by Eqs. 70 and 71 in Section 7.1.7. The linear system in Eq. 51 can be rewritten into

$$\begin{pmatrix} \mathbf{A} + \mathbf{B}_1 + \mathbf{B}_2 + \mathbf{C} + \mathbf{E} & \mathbf{D}_1 & \mathbf{F} \\ & \mathbf{D}_2^T & \\ & \mathbf{F}^T & \end{pmatrix} \begin{pmatrix} \Delta \mathbf{U}_k^{(n)} \\ \Delta \mathbf{P}_k^{(n)} \\ \Delta \boldsymbol{\Lambda}_k^{(n)} \end{pmatrix} = \begin{pmatrix} \mathbf{R}_{\mathbf{u}_t, k}^{(n)} + \mathbf{R}_{\mathbf{u}, k}^{(n)} \\ \mathbf{R}_{p, k}^{(n)} \\ \mathbf{R}_{\lambda, k}^{(n)} \end{pmatrix}. \quad (53)$$

The boundary or interface condition of $\mathbf{u}_h^{(n)}$ at $l_{v, h}$ and the point condition of $p_h^{(n)}$ at \mathcal{P}_h can be imposed by using the elimination approach, with enforcing the linear system in Eq. 53 to be definite. The variational formulation in Eq. 9 can be solved by using the procedure in Table 8.

7.1.3 Discretization of variational formulation in Eq. 20

Based on the surface finite element method and m -step BDF schemes, the variational formulation in Eq. 20 for the adjoint equations of the surface Navier-Stokes equations can be discretized into the following formulation defined on Γ_h :

for $n' = N_t - 1, N_t - 2, \dots, 0$

$$\text{find } \begin{cases} \mathbf{u}_{a, h}^{(n')} \in (\mathcal{S}_h^{(2)})^3 \text{ with } \begin{cases} \mathbf{u}_{a, h}^{(n')} - (\mathbf{u}_{a, h}^{(n')} \cdot \mathbf{n}_{\tau, h}) \mathbf{n}_{\tau, h} = \mathbf{0} \text{ at } t = n' \Delta t, \forall \mathbf{x} \in l_{v, h} \\ \mathbf{u}_{a, h}^{(N_t)} = -\frac{1}{\rho} \frac{\partial C_h}{\partial \mathbf{u}_h^{(N_t)}} \text{ at } \forall \mathbf{x} \in \Gamma_h \end{cases}, \\ p_{a, h}^{(n')} \in \mathcal{S}_h^{(1)} \text{ with } p_{a, h}^{(n')}(t, \mathbf{x}) = 0 \text{ at } t = n' \Delta t, \forall \mathbf{x} \in \mathcal{P}_h, \\ \lambda_{a, h}^{(n')} \in \mathcal{S}_h^{(2)} \text{ with } \lambda_{a, h}^{(n')} = 0 \text{ at } t = n' \Delta t, \forall \mathbf{x} \in l_{v, h}, \end{cases}$$

$$\begin{aligned} \text{such that } & \int_{\Gamma_h} \frac{\partial A_h^{(n')}}{\partial \mathbf{u}_h^{(n')}} \cdot \tilde{\mathbf{u}}_{a, h} + \frac{\partial A_h^{(n')}}{\partial \nabla_{\Gamma_h} \mathbf{u}_h^{(n')}} : \nabla_{\Gamma_h} \tilde{\mathbf{u}}_{a, h} + \frac{\partial A_h^{(n')}}{\partial p_h^{(n')}} \tilde{p}_{a, h} \\ & + \rho \frac{\theta_m \mathbf{u}_{a, h}^{(n')} - \mathbf{u}_{a, h, m}^{(n'+1)}}{\Delta t} \cdot \tilde{\mathbf{u}}_{a, h} + \rho \left[(\tilde{\mathbf{u}}_{a, h} \cdot \nabla_{\Gamma_h}) \mathbf{u}_h^{(n')} + (\mathbf{u}_h^{(n')} \cdot \nabla_{\Gamma_h}) \tilde{\mathbf{u}}_{a, h} \right] \cdot \mathbf{u}_{a, h}^{(n')} \\ & + \frac{\mu}{2} \left(\nabla_{\Gamma_h} \mathbf{u}_{a, h}^{(n')} + \nabla_{\Gamma_h} \mathbf{u}_{a, h}^{(n')T} \right) : \left(\nabla_{\Gamma_h} \tilde{\mathbf{u}}_{a, h} + \nabla_{\Gamma_h} \tilde{\mathbf{u}}_{a, h}^T \right) + \left(\alpha_h \mathbf{I} - \chi_h \frac{\partial \mathbf{b}_{p, h}^{(n')}}{\partial \mathbf{u}_h^{(n')}} \right) \mathbf{u}_{a, h}^{(n')} \cdot \tilde{\mathbf{u}}_{a, h} \\ & + \mathbf{u}_{a, h}^{(n')} \cdot \nabla_{\Gamma_h} \tilde{p}_{a, h} - p_{a, h}^{(n')} \text{div}_{\Gamma_h} \tilde{\mathbf{u}}_{a, h} + \left(\tilde{\lambda}_{a, h} \mathbf{u}_{a, h}^{(n')} + \lambda_{a, h}^{(n')} \tilde{\mathbf{u}}_{a, h} \right) \cdot \mathbf{n}_h \, d\Gamma \\ & - \int_{\partial \Gamma_h} \left(\mathbf{u}_{a, h}^{(n')} \cdot \mathbf{n}_{\tau, h} - \frac{\partial B_h^{(n')}}{\partial p_h^{(n')}} \right) \tilde{p}_{a, h} \, dl - \int_{\partial \Gamma_h \setminus l_{v, h}} \frac{\partial B_h^{(n')}}{\partial \mathbf{u}_h^{(n')}} \cdot \tilde{\mathbf{u}}_{a, h} \, dl = 0, \end{aligned}$$

$$\text{for } \forall \tilde{\mathbf{u}}_{a, h} \in (\mathcal{S}_h^{(2)})^3, \forall \tilde{p}_{a, h} \in \mathcal{S}_h^{(1)} \text{ and } \tilde{\lambda}_{a, h} \in \mathcal{S}_h^{(2)},$$

(54)

where n' is the time step number, and it is used as the superscript of the relevant variables and functions to denote the time step; $\mathbf{u}_{a, h}^{(n')}, p_{a, h}^{(n')}$ and $\lambda_{a, h}^{(n')}$ are the adjoint variables of $\mathbf{u}_h^{(n')}, p_h^{(n')}$

Algorithm 2: surface finite element solution of Eq. 9

$$\text{Set } \begin{cases} n \leftarrow 1 \\ k \leftarrow 1 \end{cases} \text{ and } \begin{cases} \mathbf{U}_k^{(n-1)} \leftarrow \mathbf{u}_0 \\ \mathbf{U}_k^{(n)} \leftarrow \mathbf{0} \\ \mathbf{P}_k^{(n)} \leftarrow \mathbf{0} \\ \mathbf{\Lambda}_k^{(n)} \leftarrow \mathbf{0} \end{cases} ;$$

loop 1 (BDF)

loop 2 (Newton iteration)

Compute $\{\mathbf{R}_{\mathbf{u}_t, k}^{(n)}, \mathbf{R}_{\mathbf{u}, k}^{(n)}, \mathbf{R}_{p, k}^{(n)}, \mathbf{R}_{\lambda, k}^{(n)}\}$ based on $\{\mathbf{U}_k^{(n)}, \mathbf{U}_k^{(n-1)}, \mathbf{U}_k^{(n-2)}, \dots, \mathbf{U}_k^{(n-m)}, \mathbf{P}_k^{(n)}, \mathbf{\Lambda}_k^{(n)}\}$;

Assemble $\{\mathbf{A}, \mathbf{B}_1, \mathbf{B}_2, \mathbf{C}, \mathbf{D}_1, \mathbf{D}_2, \mathbf{E}, \mathbf{F}\}$ based on $\{\mathbf{U}_k^{(n)}, \mathbf{P}_k^{(n)}, \mathbf{\Lambda}_k^{(n)}\}$;

Solve the definite linear system corresponding to Eq. 53 by using a PARDISO solver;

$$\text{Compute } \begin{cases} \mathbf{U}_{k+1}^{(n)} = \mathbf{U}_k^{(n)} + \Delta \mathbf{U}_k^{(n)} \\ \mathbf{P}_{k+1}^{(n)} = \mathbf{P}_k^{(n)} + \Delta \mathbf{P}_k^{(n)} \\ \mathbf{\Lambda}_{k+1}^{(n)} = \mathbf{\Lambda}_k^{(n)} + \Delta \mathbf{\Lambda}_k^{(n)} \end{cases} ;$$

$$\text{if } \begin{cases} \frac{\|\Delta \mathbf{U}_k^{(n)}\|_2}{\|\mathbf{U}_k^{(n)}\|_2} \geq 10^{-6} \\ \frac{\|\Delta \mathbf{P}_k^{(n)}\|_2}{\|\mathbf{P}_k^{(n)}\|_2} \geq 10^{-6} \\ \frac{\|\Delta \mathbf{\Lambda}_k^{(n)}\|_2}{\|\mathbf{\Lambda}_k^{(n)}\|_2} \geq 10^{-6} \end{cases}$$

$k \leftarrow k + 1$;

else

$$\text{Set } \begin{cases} \mathbf{U}^{(n)} \leftarrow \mathbf{U}_{k+1}^{(n)} \\ \mathbf{P}^{(n)} \leftarrow \mathbf{P}_{k+1}^{(n)} \\ \mathbf{\Lambda}^{(n)} \leftarrow \mathbf{\Lambda}_{k+1}^{(n)} \end{cases}, \text{ break } \mathbf{loop 2}, \text{ and continue } \mathbf{loop 1};$$

end if

end loop 2

if $n\Delta t < T$

$n \leftarrow n + 1$;

else

break **loop 1**;

end if

end loop 1

Table 8: Pseudo codes used to solve the variational formulation in Eq. 9, where $\mathbf{U}^{(n)}$, $\mathbf{P}^{(n)}$ and $\mathbf{\Lambda}^{(n)}$ are the discrete counterparts of $\mathbf{u}_h^{(n)}$, $p_h^{(n)}$ and $\lambda_h^{(n)}$, respectively; $\|\cdot\|_2$ is the operator for 2-norm of a vector.

and $\lambda_h^{(n')}$ on Γ_h at time $t = n'\Delta t$, respectively; $\tilde{\mathbf{u}}_{a,h}$, $\tilde{p}_{a,h}$ and $\tilde{\lambda}_{a,h}$ are the test functions of $\mathbf{u}_{a,h}^{(n')}$, $p_{a,h}^{(n')}$ and $\lambda_{a,h}^{(n')}$, respectively; A_h , B_h and C_h are the integration functions of the optimization objective on Γ_h ; for the m -step BDF schemes, the expression of $\mathbf{u}_{a,h}^{(n'+1)}$ is provided in Table 9 and it is determined by the linear combination of $\{\mathbf{u}_{a,h}^{(n'+1)}, \mathbf{u}_{a,h}^{(n'+2)}, \dots, \mathbf{u}_{a,h}^{(n'+m)}\}$. By setting

$$\begin{cases} F_{\mathbf{u}_{at}}^{(n')}(\tilde{\mathbf{u}}_{a,h}) := \int_{\Gamma_h} \rho \frac{1}{\Delta t} \mathbf{u}_{a,h,m}^{(n'+1)} \cdot \tilde{\mathbf{u}}_{a,h} \, d\Gamma, \\ F_{\mathbf{u}_a}^{(n')}(\tilde{\mathbf{u}}_{a,h}) := - \int_{\Gamma_h} \frac{\partial A_h^{(n')}}{\partial \mathbf{u}_h^{(n')}} \cdot \tilde{\mathbf{u}}_{a,h} + \frac{\partial A_h^{(n')}}{\partial \nabla_{\Gamma_h} \mathbf{u}_h^{(n')}} : \nabla_{\Gamma_h} \tilde{\mathbf{u}}_{a,h} \, d\Gamma - \int_{\partial\Gamma_h \setminus \Gamma_{v,h}} \frac{\partial B_h^{(n')}}{\partial \mathbf{u}_h^{(n')}} \cdot \tilde{\mathbf{u}}_{a,h} \, dl, \\ F_{p_a}^{(n')}(\tilde{p}_{a,h}) := - \int_{\Gamma_h} \frac{\partial A_h^{(n')}}{\partial p_h^{(n')}} \tilde{p}_{a,h} \, d\Gamma + \int_{\partial\Gamma_h} \frac{\partial B_h^{(n')}}{\partial p_h^{(n')}} \tilde{p}_{a,h} \, dl, \end{cases} \quad (55)$$

Eq. 54 can be equivalently transformed into

$$\begin{cases} \int_{\Gamma_h} \rho \frac{\theta_m}{\Delta t} \mathbf{u}_{a,h}^{(n')} \cdot \tilde{\mathbf{u}}_{a,h} + \rho \left[(\tilde{\mathbf{u}}_{a,h} \cdot \nabla_{\Gamma_h}) \mathbf{u}_h^{(n')} + (\mathbf{u}_h^{(n')} \cdot \nabla_{\Gamma_h}) \tilde{\mathbf{u}}_{a,h} \right] \cdot \mathbf{u}_{a,h}^{(n')} \\ + \frac{\mu}{2} \left(\nabla_{\Gamma_h} \mathbf{u}_{a,h}^{(n')} + \nabla_{\Gamma_h} \mathbf{u}_{a,h}^{(n')\top} \right) : \left(\nabla_{\Gamma_h} \tilde{\mathbf{u}}_{a,h} + \nabla_{\Gamma_h} \tilde{\mathbf{u}}_{a,h}^\top \right) + \left(\alpha_h \mathbf{I} - \chi_h \frac{\partial \mathbf{b}_{p,h}^{(n')}}{\partial \mathbf{u}_h^{(n')}} \right) \mathbf{u}_{a,h}^{(n')} \cdot \tilde{\mathbf{u}}_{a,h} \\ - p_{a,h}^{(n')} \operatorname{div}_{\Gamma_h} \tilde{\mathbf{u}}_{a,h} + \lambda_{a,h}^{(n')} \tilde{\mathbf{u}}_{a,h} \cdot \mathbf{n}_h \, d\Gamma = F_{\mathbf{u}_{at}}^{(n')}(\tilde{\mathbf{u}}_{a,h}) + F_{\mathbf{u}_a}^{(n')}(\tilde{\mathbf{u}}_{a,h}), \\ \int_{\Gamma_h} \mathbf{u}_{a,h}^{(n')} \cdot \nabla_{\Gamma_h} \tilde{p}_{a,h} \, d\Gamma - \int_{\partial\Gamma_h} \mathbf{u}_{a,h}^{(n')} \cdot \mathbf{n}_{\tau,h} \tilde{p}_{a,h} \, dl = F_{p_a}^{(n')}(\tilde{p}_{a,h}), \\ \int_{\Gamma_h} \tilde{\lambda}_{a,h} \mathbf{u}_{a,h}^{(n')} \cdot \mathbf{n}_h \, d\Gamma = 0, \end{cases} \quad (56)$$

where $F_{\mathbf{u}_a}^{(n')}(\tilde{\mathbf{u}}_{a,h})$ and $F_{p_a}^{(n')}(\tilde{p}_{a,h})$ are the sources associated with the variational formulation in Eq. 54.

n, m	$\mathbf{u}_{a,h,m}^{(n'+1)}$
$n \geq 1, m = 1$	$\mathbf{u}_{a,h}^{(n'+1)}$
$n \geq 2, m \leq 2$	$2\mathbf{u}_{a,h}^{(n'+1)} - \frac{1}{2}\mathbf{u}_{a,h}^{(n'+2)}$
$n \geq 3, m \leq 3$	$3\mathbf{u}_{a,h}^{(n'+1)} - \frac{3}{2}\mathbf{u}_{a,h}^{(n'+2)} + \frac{1}{3}\mathbf{u}_{a,h}^{(n'+3)}$
$n \geq 4, m \leq 4$	$4\mathbf{u}_{a,h}^{(n'+1)} - 3\mathbf{u}_{a,h}^{(n'+2)} + \frac{4}{3}\mathbf{u}_{a,h}^{(n'+3)} - \frac{1}{4}\mathbf{u}_{a,h}^{(n'+4)}$
$n \geq 5, m \leq 5$	$5\mathbf{u}_{a,h}^{(n'+1)} - 5\mathbf{u}_{a,h}^{(n'+2)} + \frac{10}{3}\mathbf{u}_{a,h}^{(n'+3)} - \frac{5}{4}\mathbf{u}_{a,h}^{(n'+4)} + \frac{1}{5}\mathbf{u}_{a,h}^{(n'+5)}$
$n \geq 6, m \leq 6$	$6\mathbf{u}_{a,h}^{(n'+1)} - \frac{15}{2}\mathbf{u}_{a,h}^{(n'+2)} + \frac{20}{3}\mathbf{u}_{a,h}^{(n'+3)} - \frac{15}{4}\mathbf{u}_{a,h}^{(n'+4)} + \frac{6}{5}\mathbf{u}_{a,h}^{(n'+5)} - \frac{1}{6}\mathbf{u}_{a,h}^{(n'+6)}$

Table 9: Expressions of $\mathbf{u}_{a,h,m}^{(n'+1)}$ for the m -step BDF schemes, where $\mathbf{u}_{a,h}^{(n'+1)}$ is the initial distribution of the adjoint fluidic velocity for $n' = N_t - 1$.

The discretized variational formulation for the adjoint equations of the surface Navier-Stokes equations in Eq. 54 can be solved directly, because it is linear. Based on the nodal basis $\{\psi_1^{(2)}, \psi_2^{(2)}, \dots, \psi_{N_2}^{(2)}\}$ of $\mathcal{S}_h^{(2)}$, $\mathbf{u}_{a,h}^{(n')}$ and $\lambda_{a,h}^{(n')}$ have the following transformations:

$$\left. \begin{aligned} \mathbf{u}_{a,h}^{(n')} &= \sum_{i=1}^{N_2} \mathbf{U}_{a,i}^{(n')} \psi_i^{(2)}(\mathbf{x}) \\ \lambda_{a,h}^{(n')} &= \sum_{i=1}^{N_2} \Lambda_{a,i}^{(n')} \psi_i^{(2)}(\mathbf{x}) \end{aligned} \right\} \text{at } \forall \mathbf{x} \in \Gamma_h, \quad (57)$$

where $\mathbf{U}_{a,i}^{(n')}$ and $\Lambda_{a,i}^{(n')}$ are the nodal variables of $\mathbf{u}_{a,h}^{(n')}$ and $\lambda_{a,h}^{(n')}$, respectively. Based on the

nodal basis $\{\psi_1^{(1)}, \psi_2^{(1)}, \dots, \psi_{N_1}^{(1)}\}$ of $\mathcal{S}_h^{(1)}, p_{a,h}^{(n')}$ has the following transformation:

$$p_{a,h}^{(n')} = \sum_{i=1}^{N_1} P_{a,i}^{(n')} \psi_i^{(1)}(\mathbf{x}) \text{ at } \forall \mathbf{x} \in \Gamma_h, \quad (58)$$

where $P_{a,i}^{(n')}$ is the nodal variable of $p_{a,h}^{(n')}$. By substituting Eqs. 57 and 58 into Eq. 54, and using the nodal basis of $\mathcal{S}_h^{(2)}$ and $\mathcal{S}_h^{(1)}$ as the test functions, a linear system can be derived based on the assembly rule of stiffness matrix:

$$\begin{cases} [\mathbf{A} + \mathbf{B}_1(\mathbf{U}^{(n')}) + \mathbf{B}_2(\mathbf{U}^{(n')}) + \mathbf{C}] \mathbf{U}_a^{(n')} + \mathbf{D}_1 \mathbf{P}_a^{(n')} + \mathbf{E}(\boldsymbol{\Upsilon}_p) \mathbf{U}_a^{(n')} + \\ \mathbf{F} \boldsymbol{\Lambda}_a^{(n')} = \mathbf{F}_{\mathbf{u}_{at}}^{(n')}(\mathbf{U}_a^{(n'+1)}, \mathbf{U}_a^{(n'+2)}, \dots, \mathbf{U}_a^{(n'+m)}) + \mathbf{F}_{\mathbf{u}_a}^{(n')}(\mathbf{U}^{(n')}, \mathbf{P}^{(n')}; \boldsymbol{\Upsilon}_p), \\ \mathbf{D}_2^T \mathbf{U}_a^{(n')} = \mathbf{F}_{p_a}^{(n')}(\mathbf{U}^{(n')}, \mathbf{P}^{(n')}; \boldsymbol{\Upsilon}_p), \\ \mathbf{F}^T \mathbf{U}_a^{(n')} = \mathbf{0}, \end{cases} \quad (59)$$

where $\mathbf{F}_{\mathbf{u}_{at}}^{(n')}$ depends on $\{\mathbf{U}_a^{(n'+1)}, \mathbf{U}_a^{(n'+2)}, \dots, \mathbf{U}_a^{(n'+m)}\}$, because $\mathbf{u}_{a,h,m}^{(n+1)}$ is the linear combination of $\{\mathbf{u}_{a,h}^{(n'+1)}, \mathbf{u}_{a,h}^{(n'+2)}, \dots, \mathbf{u}_{a,h}^{(n'+m)}\}$; $\mathbf{U}_a^{(n')}, \mathbf{P}_a^{(n')}$ and $\boldsymbol{\Lambda}_a^{(n')}$ are the discrete counterparts of $\mathbf{u}_{a,h}^{(n')}, p_{a,h}^{(n')}$ and $\lambda_{a,h}^{(n')}$, respectively. The correspondence between the matrixes in Eq. 59 and terms in Eqs. 55 and 56 are provided by Eqs. 72 and 73 in Section 7.1.7. The linear system in Eq. 59 can be rewritten into

$$\begin{pmatrix} \mathbf{A} + \mathbf{B}_1 + \mathbf{B}_2 + \mathbf{C} + \mathbf{E} & \mathbf{D}_1 & \mathbf{F} \\ & \mathbf{D}_2^T & \\ & \mathbf{F}^T & \end{pmatrix} \begin{pmatrix} \mathbf{U}_a^{(n')} \\ \mathbf{P}_a^{(n')} \\ \boldsymbol{\Lambda}_a^{(n')} \end{pmatrix} = \begin{pmatrix} \mathbf{F}_{\mathbf{u}_{at}}^{(n')} + \mathbf{F}_{\mathbf{u}_a}^{(n')} \\ \mathbf{F}_{p_a}^{(n')} \\ \mathbf{0} \end{pmatrix}. \quad (60)$$

The boundary or interface condition of $\mathbf{u}_{a,h}^{(n')}$ at $l_{v,h}$ and the point condition of $p_{a,h}^{(n')}$ at \mathcal{P}_h can be imposed by using the elimination approach, to enforce the linear system in Eq. 60 to be definite. The variational formulation in Eq. 20 can be solved by using the procedure in Table 10.

Algorithm 3: surface finite element solution of Eq. 20

Solve $\{\mathbf{U}^{(n)}, \mathbf{P}^{(n)}, \boldsymbol{\Lambda}^{(n)}\}$ ($n = 1, 2, \dots, N_t$) by using Algorithm 2 in Table 8;

for $n = 1, 2, \dots, N_t$

$n' = N_t - n$;

loop (BDF)

 Compute $\{\mathbf{F}_{\mathbf{u}_{at}}, \mathbf{F}_{\mathbf{u}_a}, \mathbf{F}_{p_a}\}$ based on $\{\mathbf{U}^{(n')}, \mathbf{P}^{(n')}, \boldsymbol{\Lambda}^{(n')}, \mathbf{U}_a^{(n'+1)}, \dots, \mathbf{U}_a^{(n'+m)}\}$;

 Assemble $\{\mathbf{A}, \mathbf{B}_1, \mathbf{B}_2, \mathbf{C}, \mathbf{D}_1, \mathbf{D}_2, \mathbf{E}, \mathbf{F}\}$ based on $\mathbf{U}^{(n')}$;

 Solve the definite linear system corresponding to Eq. 60 by using a PARDISO solver;

 Compute $\{\mathbf{U}_a^{(n')}, \mathbf{P}_a^{(n')}, \boldsymbol{\Lambda}_a^{(n')}\}$;

if $n' \Delta t > 0$

$n' \leftarrow n' - 1$;

else

 Break;

end if

end loop (BDF)

end for

Table 10: Pseudocode used to solve the variational formulation in Eq. 20.

7.1.4 Discretization of variational formulation in Eq. 21

Based on the surface finite element method, the variational formulation in Eq. 21 for the adjoint equation of the surface-PDE filter can be discretized into the following formulation defined on

Γ_h :

find $\gamma_{fa,h} \in \mathcal{S}_h^{(1)}$, such that

$$\begin{aligned} & \frac{1}{2N_t} \sum_{n=1}^{N_t} \int_{\Gamma_h} \left[\frac{\partial \left(A_h^{(n-1)} + A_h^{(n)} \right)}{\partial \gamma_{p,h}} + \frac{\partial \alpha_h}{\partial \gamma_{p,h}} \left(\mathbf{u}_h^{(n-1)} \cdot \mathbf{u}_{a,h}^{(n-1)} + \mathbf{u}_h^{(n)} \cdot \mathbf{u}_{a,h}^{(n)} \right) - \right. \\ & \left. \frac{\partial \chi_h}{\partial \gamma_{p,h}} \left(\mathbf{b}_{p,h}^{(n-1)} \cdot \mathbf{u}_{a,h}^{(n-1)} + \mathbf{b}_{p,h}^{(n)} \cdot \mathbf{u}_{a,h}^{(n)} \right) \right] \frac{\partial \gamma_{p,h}}{\partial \gamma_{f,h}} \tilde{\gamma}_{fa,h} \, d\Gamma + \int_{\Gamma_h} \frac{1}{T} \frac{\partial C_h}{\partial \gamma_{p,h}} \frac{\partial \gamma_{p,h}}{\partial \gamma_{f,h}} \tilde{\gamma}_{fa,h} \, d\Gamma \\ & + \int_{\Gamma_h} r_f^2 \nabla_{\Gamma_h} \gamma_{fa,h} \cdot \nabla_{\Gamma_h} \tilde{\gamma}_{fa,h} + \gamma_{fa,h} \tilde{\gamma}_{fa,h} \, d\Gamma = 0, \text{ for } \forall \tilde{\gamma}_{fa,h} \in \mathcal{S}_h^{(1)}, \end{aligned} \quad (61)$$

where $\gamma_{fa,h}$ is discretized adjoint variable of the filtered design variable on Γ_h ; the time integration is implemented by using a trapezoid method.

Based on the nodal basis $\{\psi_1^{(1)}, \psi_2^{(1)}, \dots, \psi_{N_1}^{(1)}\}$ of $\mathcal{S}_h^{(1)}$, $\gamma_{fa,h}$ has the following transformation:

$$\gamma_{fa,h} = \sum_{i=1}^{N_1} \Upsilon_{fa,h,i} \psi_i^{(1)}(\mathbf{x}) \text{ at } \forall \mathbf{x} \in \Gamma_h, \quad (62)$$

where $\Upsilon_{fa,h,i}$ is the nodal variable of $\gamma_{fa,h}$. By substituting Eq. 62 into Eq. 61, and using the nodal basis of $\mathcal{S}_h^{(1)}$ as the test functions, a linear system can be derived based on the assembly rule of stiffness matrix:

$$(\mathbf{K} + \mathbf{N}) \mathbf{\Upsilon}_{fa} = \mathbf{F}_{\gamma_{fa}} \left(\mathbf{U}^{(1)}, \dots, \mathbf{U}^{(N_t)}, \mathbf{P}^{(1)}, \dots, \mathbf{P}^{(N_t)}, \mathbf{U}_a^{(1)}, \dots, \mathbf{U}_a^{(N_t)}; \mathbf{\Upsilon}_f \right), \quad (63)$$

where $\mathbf{\Upsilon}_{fa}$ is the discrete counterpart of $\gamma_{fa,h}$. The correspondence between the matrixes in Eq. 63 and terms in Eq. 61 are provided in Section 7.1.7. The variational formulation in Eq. 44 can be solved by using a PARDISO solver [66].

7.1.5 Computation of adjoint sensitivity in Eq. 19

Based on the finite element space in Eq. 40 and adjoint sensitivity in Eq. 19, the adjoint sensitivity of J on Γ_h is expressed as

$$\Delta J_h = -T \int_{\Gamma_h} \gamma_{fa,h} \delta \gamma_h \, d\Gamma, \quad (64)$$

where $\delta \gamma_h \in \mathcal{S}_h^{(1)}$ is the first order variational of γ_h . Based on Eq. 43, $\delta \gamma_h$ is expressed as

$$\delta \gamma_h = \sum_{i=1}^{N_1} \Delta \Upsilon_{h,i} \psi_i^{(1)}(\mathbf{x}). \quad (65)$$

By substituting Eqs. 62 and 65 into Eq. 64, the discretized adjoint sensitivity in Eq. 64 can be transformed into

$$\frac{\Delta J_h}{\Delta \mathbf{\Upsilon}} = -T \mathbf{N} \mathbf{\Upsilon}_{fa}, \quad (66)$$

where $\Delta \mathbf{\Upsilon}$ is the discrete counterpart of $\delta \gamma_h$.

7.1.6 Computation of adjoint sensitivity in Eq. 22

Based on the finite element space in Eq. 40 and adjoint sensitivity in Eq. 22, the adjoint sensitivity of v on Γ_h is expressed as

$$\Delta v_h = -\frac{1}{|\Gamma_h|} \int_{\Gamma_h} \gamma_{fa,h} \delta \gamma_h \, d\Gamma. \quad (67)$$

By substituting Eqs. 62 and 65 into Eq. 67, the discretized adjoint sensitivity in Eq. 67 can be transformed into

$$\frac{\Delta v_h}{\Delta \mathbf{\Upsilon}} = -\frac{\mathbf{N} \mathbf{\Upsilon}_{fa}}{\mathbf{1}^T \mathbf{N} \mathbf{1}}, \quad (68)$$

where $\mathbf{1}$ is the $N_1 \times 1$ column vector with all elements equal to 1; $|\Gamma_h|$ is computed as $\mathbf{1}^T \mathbf{N} \mathbf{1}$.

7.1.7 Notifications

The formulations in Section 7.1.2-7.1.5 can degenerate into the ones for the steady surface flows by setting the terminal time to be $T = 1$, taking the limitation of the related expressions with $\Delta t \rightarrow +\infty$ and reducing the expression in the averaged form of $\frac{1}{2N_t} \sum_{n=1}^{N_t} \int_{\Gamma_h} \cdot d\Gamma$. By using a similar discretization approach for the steady surface flows, the stabilized variational formulations and the adjoint formulations in Section 4.3 can be discretized on the finite element space in Eq. 40.

In the derived linear systems (Eqs. 44, 53, 60 and 63) and the discretized adjoint sensitivities (Eqs. 66 and 68), several sub-matrixes can be reused to avoid reassembly operations. This can effectively reduce the CPU-time cost during the implementation of the surface finite element solution. The correspondence between the finite element matrixes of the linear systems and the terms of the variational formulations defined on the discretized 2-manifold are provided as follows. The correspondence between the matrixes in Eq. 44 and the terms in Eq. 43 can be described as

$$\left\{ \begin{array}{l} \mathbf{K}\Upsilon_f \longleftrightarrow \int_{\Gamma_h} r_f^2 \nabla_{\Gamma_h} \gamma_{f,h} \cdot \nabla_{\Gamma_h} \tilde{\gamma}_{f,h} d\Gamma, \\ \mathbf{N}\Upsilon_f \longleftrightarrow \int_{\Gamma_h} \gamma_{f,h} \tilde{\gamma}_{f,h} d\Gamma, \\ \mathbf{N}\Upsilon \longleftrightarrow \int_{\Gamma_h} \gamma_h \tilde{\gamma}_{f,h} d\Gamma. \end{array} \right. \quad (69)$$

The correspondence between the matrixes in Eq. 51 and the terms in Eqs. 47 and 48 can be described as

$$\left\{ \begin{array}{l} \mathbf{R}_{\mathbf{u}_t, k}^{(n)} \left(\mathbf{U}_k^{(n)}, \mathbf{U}_k^{(n-1)}, \dots, \mathbf{U}_k^{(n-m)} \right) \longleftrightarrow R_{\mathbf{u}_t, k}^{(n)} (\tilde{\mathbf{u}}_h), \\ \mathbf{R}_{\mathbf{u}, k}^{(n)} \left(\mathbf{U}_k^{(n)}, \mathbf{P}_k^{(n)}, \boldsymbol{\Lambda}_k^{(n)}; \Upsilon_p \right) \longleftrightarrow R_{\mathbf{u}, k}^{(n)} (\tilde{\mathbf{u}}_h), \\ \mathbf{R}_{p, k}^{(n)} \left(\mathbf{U}_k^{(n)} \right) \longleftrightarrow R_{p, k}^{(n)} (\tilde{p}_h), \\ \mathbf{R}_{\lambda, k}^{(n)} \left(\mathbf{U}_k^{(n)} \right) \longleftrightarrow R_{\lambda, k}^{(n)} (\tilde{\lambda}_h), \end{array} \right. \quad (70)$$

and

$$\left\{ \begin{array}{l} \mathbf{A}\Delta\mathbf{U}_k^{(n)} \longleftrightarrow \int_{\Gamma_h} \rho \frac{\theta_m}{\Delta t} \delta \mathbf{u}_{h,k}^{(n)} \cdot \tilde{\mathbf{u}}_h d\Gamma, \\ \mathbf{B}_1 \left(\mathbf{U}_k^{(n)} \right) \Delta\mathbf{U}_k^{(n)} \longleftrightarrow \int_{\Gamma_h} \rho \left[\left(\mathbf{u}_{h,k}^{(n)} \cdot \nabla_{\Gamma_h} \right) \delta \mathbf{u}_{h,k}^{(n)} \right] \cdot \tilde{\mathbf{u}}_h d\Gamma, \\ \mathbf{B}_2 \left(\mathbf{U}_k^{(n)} \right) \Delta\mathbf{U}_k^{(n)} \longleftrightarrow \int_{\Gamma_h} \rho \left[\left(\delta \mathbf{u}_{h,k}^{(n)} \cdot \nabla_{\Gamma_h} \right) \mathbf{u}_{h,k}^{(n)} \right] \cdot \tilde{\mathbf{u}}_h d\Gamma, \\ \mathbf{C}\Delta\mathbf{U}_k^{(n)} \longleftrightarrow \int_{\Gamma_h} \frac{\mu}{2} \left(\nabla_{\Gamma_h} \delta \mathbf{u}_{h,k}^{(n)} + \nabla_{\Gamma_h} \delta \mathbf{u}_{h,k}^{(n)\text{T}} \right) : \left(\nabla_{\Gamma_h} \tilde{\mathbf{u}}_h + \nabla_{\Gamma_h} \tilde{\mathbf{u}}_h^{\text{T}} \right) d\Gamma, \\ \mathbf{D}_1 \Delta \mathbf{P}_k^{(n)} \longleftrightarrow \int_{\Gamma_h} -\delta p_{h,k}^{(n)} \text{div}_{\Gamma_h} \tilde{\mathbf{u}}_h d\Gamma, \\ \mathbf{E} \left(\Upsilon_p \right) \Delta\mathbf{U}_k^{(n)} \longleftrightarrow \int_{\Gamma_h} \left(\alpha_h \delta \mathbf{u}_{h,k}^{(n)} - \chi_h \frac{\partial \mathbf{b}_{p,h}^{(n)}}{\partial \mathbf{u}_{h,k}^{(n)}} \delta \mathbf{u}_{h,k}^{(n)} \right) \cdot \tilde{\mathbf{u}}_h d\Gamma, \\ \mathbf{F}\Delta\boldsymbol{\Lambda}_k^{(n)} \longleftrightarrow \int_{\Gamma_h} \delta \lambda_{h,k}^{(n)} (\tilde{\mathbf{u}}_h \cdot \mathbf{n}_h) d\Gamma, \\ \mathbf{D}_2^{\text{T}} \Delta\mathbf{U}_k^{(n)} \longleftrightarrow \int_{\Gamma_h} \delta \mathbf{u}_{h,k}^{(n)} \cdot \nabla_{\Gamma_h} \tilde{p}_h d\Gamma - \int_{\partial\Gamma_h \setminus \Gamma_{v,h}} \delta \mathbf{u}_{h,k}^{(n)} \cdot \mathbf{n}_{\tau,h} \tilde{p}_h dl, \\ \mathbf{F}^{\text{T}} \Delta\mathbf{U}_k^{(n)} \longleftrightarrow \int_{\Gamma_h} \tilde{\lambda}_h \left(\delta \mathbf{u}_{h,k}^{(n)} \cdot \mathbf{n}_h \right) d\Gamma. \end{array} \right. \quad (71)$$

The correspondence between the matrixes in Eq. 59 and the terms in Eqs. 55 and 56 can be described as

$$\left\{ \begin{array}{l} \mathbf{F}_{\mathbf{u}_{at}}^{(n')} \left(\mathbf{U}_a^{(n'+1)}, \mathbf{U}_a^{(n'+2)}, \dots, \mathbf{U}_a^{(n'+m)} \right) \longleftrightarrow F_{\mathbf{u}_{at}}^{(n')} (\tilde{\mathbf{u}}_{a,h}), \\ \mathbf{F}_{\mathbf{u}_a}^{(n')} \left(\mathbf{U}^{(n')}, \mathbf{P}^{(n')}; \Upsilon_p \right) \longleftrightarrow F_{\mathbf{u}_a}^{(n')} (\tilde{\mathbf{u}}_{a,h}), \\ \mathbf{F}_{p_a}^{(n')} \left(\mathbf{U}^{(n')}, \mathbf{P}^{(n')}; \Upsilon_p \right) \longleftrightarrow F_{p_a}^{(n')} (\tilde{p}_{a,h}), \end{array} \right. \quad (72)$$

and

$$\left\{ \begin{array}{l}
\mathbf{A}\mathbf{U}_a^{(n')} \longleftrightarrow \int_{\Gamma_h} \rho \frac{\theta_m}{\Delta t} \mathbf{u}_{a,h}^{(n')} \cdot \tilde{\mathbf{u}}_{a,h} \, d\Gamma, \\
\mathbf{B}_1(\mathbf{U}^{(n')}) \mathbf{U}_a^{(n')} \longleftrightarrow \int_{\Gamma_h} \rho \left[\left(\mathbf{u}_h^{(n')} \cdot \nabla_{\Gamma_h} \right) \tilde{\mathbf{u}}_{a,h} \right] \cdot \mathbf{u}_{a,h}^{(n')} \, d\Gamma, \\
\mathbf{B}_2(\mathbf{U}^{(n')}) \mathbf{U}_a^{(n')} \longleftrightarrow \int_{\Gamma_h} \rho \left[\left(\tilde{\mathbf{u}}_{a,h} \cdot \nabla_{\Gamma_h} \right) \mathbf{u}_h^{(n')} \right] \cdot \mathbf{u}_{a,h}^{(n')} \, d\Gamma, \\
\mathbf{C}\mathbf{U}_a^{(n')} \longleftrightarrow \int_{\Gamma_h} \frac{\mu}{2} \left(\nabla_{\Gamma_h} \mathbf{u}_{a,h}^{(n')} + \nabla_{\Gamma_h} \mathbf{u}_{a,h}^{(n')\text{T}} \right) : \left(\nabla_{\Gamma_h} \tilde{\mathbf{u}}_{a,h} + \nabla_{\Gamma_h} \tilde{\mathbf{u}}_{a,h}^{\text{T}} \right) \, d\Gamma, \\
\mathbf{D}_1 \mathbf{P}_a^{(n')} \longleftrightarrow \int_{\Gamma_h} -p_{a,h}^{(n')} \operatorname{div}_{\Gamma_h} \tilde{\mathbf{u}}_{a,h} \, d\Gamma, \\
\mathbf{E}(\Upsilon_p) \mathbf{U}_a^{(n')} \longleftrightarrow \int_{\Gamma_h} \left(\alpha_h \mathbf{I} - \chi_h \frac{\partial \mathbf{b}_{p,h}^{(n')}}{\partial \mathbf{u}_h^{(n')}} \right) \mathbf{u}_{a,h}^{(n')} \cdot \tilde{\mathbf{u}}_{a,h} \, d\Gamma, \\
\mathbf{F}\Lambda_a^{(n')} \longleftrightarrow \int_{\Gamma_h} \lambda_{a,h}^{(n')} \tilde{\mathbf{u}}_{a,h} \cdot \mathbf{n}_h \, d\Gamma, \\
\mathbf{D}_2^{\text{T}} \mathbf{U}_a^{(n')} \longleftrightarrow \int_{\Gamma_h} \mathbf{u}_{a,h}^{(n')} \cdot \nabla_{\Gamma_h} \tilde{p}_{a,h} \, d\Gamma - \int_{\partial\Gamma_h} \mathbf{u}_{a,h}^{(n')} \cdot \mathbf{n}_{\tau,h} \tilde{p}_{a,h} \, dl, \\
\mathbf{F}^{\text{T}} \mathbf{U}_a^{(n')} \longleftrightarrow \int_{\Gamma_h} \tilde{\lambda}_{a,h} \mathbf{u}_{a,h}^{(n')} \cdot \mathbf{n}_h \, d\Gamma.
\end{array} \right. \quad (73)$$

The correspondence between the matrixes in Eq. 63 and the terms in Eq. 61 can be described as

$$\left\{ \begin{array}{l}
\mathbf{K}\Upsilon_f \longleftrightarrow \int_{\Gamma_h} r_f^2 \nabla_{\Gamma_h} \gamma_{fa,h} \cdot \nabla_{\Gamma_h} \tilde{\gamma}_{fa,h} \, d\Gamma, \\
\mathbf{N}\Upsilon_f \longleftrightarrow \int_{\Gamma_h} \gamma_{fa,h} \tilde{\gamma}_{fa,h} \, d\Gamma, \\
\mathbf{F}_{\gamma_{fa}} \longleftrightarrow \frac{1}{2N_t} \sum_{n=1}^{N_t} \int_{\Gamma_h} \left[\frac{\partial \left(A_h^{(n-1)} + A_h^{(n)} \right)}{\partial \gamma_{p,h}} + \frac{\partial \alpha_h}{\partial \gamma_{p,h}} \left(\mathbf{u}_h^{(n-1)} \cdot \mathbf{u}_{a,h}^{(n-1)} + \mathbf{u}_h^{(n)} \cdot \mathbf{u}_{a,h}^{(n)} \right) \right. \\
\quad \left. - \frac{\partial \chi_h}{\partial \gamma_{p,h}} \left(\mathbf{b}_{p,h}^{(n-1)} \cdot \mathbf{u}_{a,h}^{(n-1)} + \mathbf{b}_{p,h}^{(n)} \cdot \mathbf{u}_{a,h}^{(n)} \right) \right] \frac{\partial \gamma_{p,h}}{\partial \gamma_{f,h}} \tilde{\gamma}_{fa,h} \, d\Gamma \\
\quad + \int_{\Gamma_h} \frac{1}{T} \frac{\partial C_h}{\partial \gamma_{p,h}} \frac{\partial \gamma_{p,h}}{\partial \gamma_{f,h}} \tilde{\gamma}_{fa,h} \, d\Gamma.
\end{array} \right. \quad (74)$$

References

- [1] Y. Kwon, N. Patankar, J. Choi, J. Lee, Design of surface hierarchy for extreme hydrophobicity, *Langmuir* 2009, **25**, 6129-6136.
- [2] S. S. Sretharan, *Optimal control of viscous flow*, SIAM, Philadelphia, 1998.
- [3] H. Thimbleby, The Leidenfrost phenomenon, *Physics Education* 1989, **24**, 300-303.
- [4] T. Baumgart, S. T. Hess, W. W. Webb, Imaging coexisting fluid domains in biomembrane models coupling curvature and line tension, *Nature*, 2003, **425**, 821-824.
- [5] G. Whitesides, A. Stroock, Flexible methods for microfluidics, *Physics Today* 2001, **54**, 42-47.
- [6] J. Berthier, K. A. Brakke, E. Berthier, *Open microfluidics*, Wiley-Scrivener, 2016.
- [7] M. Bendsøe, N. Kikuchi, Generating optimal topologies in optimal design using a homogenization method, *Comput. Methods Appl. Mech. Eng.* 1988, **71**, 197-224.
- [8] M. P. Bendsøe, O. Sigmund, *Topology optimization-theory, methods and applications*, Springer, Berlin, 2003.
- [9] T. Borrvall, J. Petersson, Topology optimization of fluid in Stokes flow, *Int. J. Numer. Methods Fluids* 2003, **41**, 77-107.
- [10] A. Gersborg-Hansen, M.P. Bendsøe, O. Sigmund, Topology optimization of heat conduction problems using the finite volume method, *Struct. Multidisc. Optim.* 2006, **31**, 251-259.

- [11] J. Guest, J. Prévost, Topology optimization of creeping fluid flows using a Darcy-Stokes finite element, *Int. J. Numer. Methods Eng.* 2006, 66, 461-484.
- [12] S. Kreissl, G. Pingen, K. Maute, An explicit level-set approach for generalized shape optimization of fluids with the lattice Boltzmann method, *Int. J. Numer. Meth. Fluids* 2011, **65**, 496-519.
- [13] Y. Deng, Z. Liu, P. Zhang, Y. Liu, Y. Wu, Topology optimization of unsteady incompressible Navier-Stokes flows, *J. Comput. Phys.* 2011, **230**, 6688-6708.
- [14] Y. Deng, Z. Liu, J. Wu, Y. Wu, Topology optimization of steady Navier-Stokes flow with body force, *Comput. Methods Appl. Mech. Engrg.* 2013, 255, 306-321.
- [15] Y. Deng, Z. Liu, Y. Wu, Topology optimization of steady and unsteady incompressible Navier-Stokes flows driven by body forces, *Struct. Multidisc. Optim.* 2013, 47, 555-570.
- [16] C. B. Dilgen, S. B. Dilgen, D. R. Fuhrman, O. Sigmund, B. S. Lazarov, Topology optimization of turbulent flows, *Comput. Methods Appl. Mech. Eng.*, 2018, 331, 363-393.
- [17] G. H. Yoon, Topology optimization for turbulent flow with Spalart-Allmaras model, *Comput. Methods Appl. Mech. Eng.*, 2016, 303, 288-311.
- [18] Y. Deng, Z. Liu, Y. Wu, Topology optimization of capillary, two-phase flow problems, *Commun. Comput. Phys.*, 2017, 22, 1413-1438.
- [19] M. M. Gregersen, F. Okkels, M. Z. Bazant, H. Bruus, Topology and shape optimization of induced-charge electro-osmotic micropumps, *New J. Phys.* 2009, **11**, 075019.
- [20] Y. Deng, T. Zhou, Z. Liu, Y. Wu, S. Qian, J. G. Korvink, Topology optimization of electrode patterns for electroosmotic micromixer, *Int. J. Heat Mass Tran.* 2018, **126**, 1299-1315.
- [21] G. Pingen, K. Maute, Optimal design for non-Newtonian flows using a topology optimization approach, *Comput. Math. Appl.* 2010, **59**, 2340-2350.
- [22] D. H. Alonso, J. S. R. Saenz, E. C. N. Silva, Optimal design for non-Newtonian flows using a topology optimization approach, *Struct. Multidisc. Optim.* 2020, <https://doi.org/10.1007/s00158-020-02499-2>.
- [23] J. Alexandersen, C. S. Andreasen, A review of topology optimisation for fluid-based problems, *Fluids* 2020, **5**, 29.
- [24] N. Vermaak, G. Michailidis, G. Parry, R. Estevez, G. Allaire, Y. Bréchet, Material interface effects on the topology optimization of multi-phase structures using a level set method, *Struct. Multidisc. Optim.* 2014, 50, 623-644.
- [25] O. Sigmund, S. Torquato, Design of materials with extreme thermal expansion using a three-phase topology optimization method, *J. Mech. Phys. Solids* 1997, 45, 1037-1067.
- [26] T. Gao, W. Zhang, A mass constraint formulation for structural topology optimization with multiphase materials, *Int. J. Numer. Meth. Engng.* 2011, 88, 774-796.
- [27] Y. J. Luo, Z. Kang, Z. F. Yue, Maximal stiffness design of two-material structures by topology optimization with nonprobabilistic reliability, *AIAA J.* 2012, 50, 1993-2003.
- [28] M. Y. Wang, X. M. Wang, "Color" level sets: a multi-phase method for structural topology optimization with multiple materials, *Comput. Methods Appl. Mech. Eng.* 2004, 193, 469-496.
- [29] S. W. Zhou, M. Y. Wang, Multimaterial structural topology optimization with a generalized Cahn-Hilliard model of multiphase transition, *Struct. Multidisc. Optim.* 2007, 33, 89-111.
- [30] P. Vogiatzis, M. Ma, S. Chen, X. Gu, Computational design and additive manufacturing of periodic conformal metasurfaces by synthesizing topology optimization with conformal mapping, *Comput. Methods Appl. Mech. Engrg.* 2018, **328**, 477-497.
- [31] L. Krog, N. Olhoff, Optimum topology and reinforcement design of disk and plate structures with multiple stiffness and eigenfrequency objectives, *Comput. Struct.* 1996, 72, 535-63.
- [32] R. Anzola, J. Canales, J. A. Tárrago, J. Rasmussen, An integrated approach for shape and topology optimization of shell structures, *Comput. Struct.* 2002, 80, 449-458.
- [33] B. Hassani, S. M. Tavakkoli, H. Ghasemnejad, Simultaneous shape and topology optimization of shell structures, *Struct. Multidisc. Optim.* 2013, 48, 221-233.
- [34] I. Lochner-Aldinger, A. Schumacher, Homogenization method. In: S. Adriaenssens, P. Block, D. Veenendaal, C. Williams (eds) *Shell structures for architecture-form finding and optimization*, Routledge, New York, 2014.
- [35] A. Clausen, E. Andreassen, O. Sigmund, Topology optimization of 3D shell structures with porous infill, *Acta Mech. Sinica* 2017, 33, 778-791.
- [36] R. Dienemann, A. Schumacher, S. Fiebig, Topology optimization for finding shell structures manufactured by deep drawing, *Struct. Multidisc. Optim.* 2017, 56, 473-485.

- [37] G. H. Yoon, Topology optimization for stationary fluid-structure interaction problems using a new monolithic formulation, *Int. J. Numer. Meth. Engng* 2010, 82, 591-616.
- [38] C. Lundgaard, J. Alexandersen, M. Zhou, C. S. Andreasen, O. Sigmund, Revisiting density-based topology optimization for fluid-structure-interaction problems, *Struct. Multidisc. Optim.* 2018, 58, 969-995.
- [39] C. S. Andreasen, A framework for topology optimization of inertial microfluidic particle manipulators, *Struct. Multidisc. Optim.* 2020, <https://doi.org/10.1007/s00158-019-02483-5>.
- [40] N. Aulig, I. Lepenies, *A topology optimization interface for LS-DYNA*. In: 11. LS-DYNA Forum, Ulm, 2012.
- [41] R. Behrou, M. Lawry, K. Maute, Level set topology optimization of structural problems with interface cohesion, *Int. J. Numer. Meth. Engng* 2017, 112, 990-1016.
- [42] M. Rauli, K. Maute, Topology optimization of electrostatically actuated microsystems, *Struct. Multidisc. Optim.* 2005, 30, 342-359.
- [43] Y. Deng, D. Mager, Y. Bai, T. Zhou, Z. Liu, L. Wen, Y. Wu, J. G. Korvink, Inversely designed micro-textures for robust Cassie-Baxter mode of super-hydrophobicity, *Comput. Methods Appl. Mech. Engrg.* 2018, 341, 113-132.
- [44] Y. Deng, Z. Liu, Y. Wang, H. Duan, J. G. Korvink, Micro-textures inversely designed with overlaid-lithography manufacturability for wetting behavior in Cassie-Baxter status, *Appl. Math. Model.* 2019, 74, 621-640.
- [45] Y. Deng, W. Zhang, Z. Liu, J. Zhu, J. G. Korvink, Fiber bundle topology optimization of hierarchical microtextures for wetting behavior in Cassie-Baxter mode, *Struct. Multidisc. Optim.* 2020, DOI: 10.1007/s00158-020-02558-8.
- [46] Y. Deng, Z. Liu, J. G. Korvink, Topology optimization on two-dimensional manifolds, *Comput. Methods Appl. Mech. Engrg.* 2020, 364, 112937.
- [47] L. Scriven, Dynamics of a fluid interface equation of motion for Newtonian surface fluids, *Chem. Eng. Sci.* 1960, 12, 98-108.
- [48] M. Arroyo, A. DeSimone, Relaxation dynamics of fluid membranes, *Phys. Rev. E* 2009, 79, 031915.
- [49] H. Brenner, *Interfacial transport processes and rheology*, Elsevier, 2013.
- [50] M. Rahimi, A. DeSimone, M. Arroyo, Curved fluid membranes behave laterally as effective viscoelastic media, *Soft Matter* 2013, 9, 11033-11045.
- [51] P. Rangamani, A. Agrawal, K. K. Mandadapu, G. Oster, D. J. Steigmann, Interaction between surface shape and intra-surface viscous flow on lipid membranes, *Biomech. Model. Mechan.* 2013, 1-13.
- [52] J. C. Slattery, L. Sagis, E. S. Oh, *Interfacial transport phenomena*, Springer Science & Business Media, 2007.
- [53] T. P. Fries, Higher-order surface FEM for incompressible Navier-Stokes flows on manifolds, *Int. J. Numer. Meth. Fl.* 2018, 88, 55-78.
- [54] S. Reuther, A. Voigt, Solving the incompressible surface Navier-Stokes equation by surface finite elements, *Phys. Fluids* 2018, 30, 012107.
- [55] L. Scriven, Dynamics of a fluid interface equation of motion for Newtonian surface fluids, *Chem. Eng. Sci.* 1960, 12, 98-108.
- [56] A. Reusken, Y. Zhang, Numerical simulation of incompressible two-phase flows with a Boussinesq-Scriven surface stress tensor, *Int. J. Numer. Meth. Fl.* 2013, 73, 1042-1058.
- [57] B. Lazarov, O. Sigmund, Filters in topology optimization based on Helmholtz type differential equations, *Int. J. Numer. Methods Engrg.* 2011, 86, 765-781.
- [58] F. Wang, B. S. Lazarov, O. Sigmund, On projection methods, convergence and robust formulations in topology optimization, *Struct. Multidiscip. Optim.* 2011, 43, 767-784.
- [59] J. Guest, J. Prévost, T. Belytschko, Achieving minimum length scale in topology optimization using nodal design variables and projection functions, *Int. J. Numer. Methods Engrg.* 2004, 61, 238-254.
- [60] M. Hinze, R. Pinnau, M. Ulbrich, S. Ulbrich, *Optimization with PDE constraints*, Springer, Berlin, 2009.
- [61] G. Dziuk, C. M. Elliott, Finite element methods for surface PDEs, *Acta Numer.*, 2013, 22, 289-396.
- [62] U. M. Ascher, L. R. Petzold, *Computer methods for ordinary differential equations and differential-algebraic equations*, SIAM, Philadelphia, 1998, ISBN 0-89871-412-5.

- [63] H. C. Elman, D. J. Silvester, A. J. Wathen, *Finite elements and fast iterative solvers: with applications in incompressible fluid dynamics*, Oxford University Press, 2006.
- [64] K. Svanberg, The method of moving asymptotes: a new method for structural optimization, *Int. J. Numer. Meth. Engrg.* 1987, 24, 359-373.
- [65] E. Süli, D. Mayers, *An introduction to numerical analysis*, Cambridge University Press, 2003, ISBN 0-521-00794-1.
- [66] <https://www.pardiso-project.org/>.
- [67] C. S. Andreasen, A. R. Gersborg, O. Sigmund, Topology optimization of microfluidic mixers, *Int. J. Numer. Meth. Fl.* 2009, 61, 498-513.
- [68] Y. Deng, Z. Liu, Ping Zhang, Y. Liu, Q. Gao, Y. Wu, A flexible layout design method for passive micromixers, *Biomed. Microdevices* 2012, 14, 929-945.
- [69] F. Brezzi and J. Pitkäranta, *On the Stabilization of Finite Element Approximations of the Stokes Equations*, Vieweg+Teubner Verlag, Wiesbaden, 1984.
- [70] J. Donea, A. Hureta, *Finite Element Methods for Flow Problems*, Wiley, West Sussex, 2003.